Monthly Notices
of the
ROYAL ASTRONOMICAL SOCIETY

MNRAS **483,** 790–805 (2019)
Advance Access publication 2018 November 10

doi:10.1093/mnras/sty3044

# The modified gravity light-cone simulation project – I. Statistics of matter and halo distributions

Christian Arnold [1]★ Pablo Fosalba,[2,3] Volker Springel [4,5,6] Ewald Puchwein[7] and Linda Blot [2,3]

[1] *Institute for Computational Cosmology, Department of Physics, Durham University, South Road, Durham DH1 3LE, UK*
[2] *Institute of Space Sciences (ICE, CSIC), Campus UAB, Carrer de Can Magrans, s/n, E-08193 Barcelona, Spain*
[3] *Institut d'Estudis Espacials de Catalunya (IEEC), Carrer Gran Capità 2-4, E-08193 Barcelona, Spain*
[4] *Heidelberger Institut für Theoretische Studien, Schloss-Wolfsbrunnenweg 35, D-69118 Heidelberg, Germany*
[5] *Zentrum für Astronomie der Universität Heidelberg, Astronomisches Recheninstitut, Mönchhofstr. 12-14, D-69120 Heidelberg, Germany*
[6] *Max-Planck-Institut für Astrophysik, Karl-Schwarzschild-Str 1, D-85741 Garching, Germany*
[7] *Kavli Institute for Cosmology, Cambridge and Institute of Astronomy, University of Cambridge, Madingley Road, Cambridge CB3 0HA, UK*

Accepted 2018 November 5. Received 2018 November 5; in original form 2018 May 24

## ABSTRACT

We introduce a set of four very high resolution cosmological simulations exploring $f(R)$ gravity, with $2048^3$ particles in 768 and 1536 $h^{-1}$ Mpc simulation boxes, for $|\bar{f}_{R0}| = 10^{-5}$ and $\Lambda$ cold dark matter ($\Lambda$CDM), making the set the largest simulations of $f(R)$ gravity to date. To mimic real observations, the simulations include a continuous 2D- and 3D-light-cone output dedicated to study lensing and clustering statistics. We present a detailed analysis and resolution study for the matter power spectrum in $f(R)$ gravity over a wide range of scales. We also analyse the angular matter power spectrum and lensing convergence on the light-cone. In addition, we investigate the impact of modified gravity on the halo mass function, matter, and halo autocorrelation functions, linear halo bias, and the concentration–mass relation. The impact of $f(R)$ gravity is generally larger on smaller scales and smaller redshift. Comparing our simulations to state-of-the-art hydrodynamical simulations, we confirm a degeneracy between $f(R)$ gravity and baryonic feedback in the matter power spectrum on small scales, but also find that scales around $k = 1\,h\,\mathrm{Mpc}^{-1}$ are promising to distinguish both effects. The lensing convergence power spectrum is increased in $f(R)$ gravity. Numerical fits are in good agreement with our simulations for both standard and modified gravity, but tend to overestimate their relative difference on non-linear scales. The halo bias is lower in $f(R)$ gravity, whereas halo concentrations are increased for unscreened haloes.

**Key words:** methods: numerical – cosmology: theory.

## 1 INTRODUCTION

The question of the nature of gravity is one of the most profound problems in fundamental physics. Although Einstein's General Relativity (GR) has been confirmed to remarkably high precision on small scales (Will 2014), there are very few tests of the theory on cosmological scales. Upcoming large-scale structure surveys like *Euclid* (Laureijs et al. 2011) or Large Synoptic Survey Telescope (LSST; LSST Science Collaboration 2009) aim to perform such tests by observing the large-scale matter distribution of the Universe. In order to fully explore their capacities it is crucial to obtain a detailed understanding of how possible deviations from GR would alter cosmic structure formation and with that the observable large-scale structure of the universe.

In this work we present a set of high-resolution cosmological simulations in $f(R)$ gravity (Buchdahl 1970), which is a possible alternative to GR. $f(R)$ gravity has an impact on structure formation in low-density environments through a factor of 4/3 increased gravitational forces (see e.g. Joyce et al. 2015, for a recent review). For a suitable choice of parameters it nevertheless still passes local tests of gravity (Hu & Sawicki 2007) as these increased forces are screened in dense environments through the chameleon screening mechanism (Khoury & Weltman 2004). The theory predicts a speed of gravitational waves that is identical to the speed of light (Lombriser & Taylor 2016; Ezquiaga & Zumalacárregui 2017; Lombriser & Lima 2017; Sakstein & Jain 2017) and therefore passes the constraints of Abbott et al. (2017) making it an ideal theory to explore

★ E-mail: christian.arnold@durham.ac.uk

how the possible deviations from GR mentioned above might be observable in upcoming surveys.

In addition to providing insight into what plausible alternatives to GR could look like, $f(R)$ gravity can – among other modified gravity theories – explain the late time accelerated expansion of the Universe without a cosmological constant $\Lambda$. As the origin of $\Lambda$ is theoretically not well motivated and poorly understood, such modified gravity theories have become a very active field of research (Sotiriou & Faraoni 2010; Nojiri & Odintsov 2011; Clifton et al. 2012; Hassan & Rosen 2012; Joyce et al. 2015; Nojiri, Odintsov & Oikonomou 2017). The predicted gravitational wave speed in many of those theories is nevertheless in tension with recent observational data (Abbott et al. 2017).

The chameleon mechanism that is essential to screen the modifications to GR in high-density environments induces a highly non-linear behaviour of the equations underlying the theory. Therefore, analytic approaches to cosmic structure formation in $f(R)$ gravity are even more limited than for GR. Cosmological simulations in modified gravity can on the other hand fully describe these non-linearities and have therefore become the primary tool to study cosmic structure formation in modified gravity (Oyaizu 2008; Li et al. 2012; Puchwein, Baldi & Springel 2013; Llinares, Mota & Winther 2014).

Cosmological simulation works on $f(R)$ gravity include studies of halo and matter statistics (Schmidt 2010; Li & Hu 2011; Zhao, Li & Koyama 2011; Hellwing et al. 2013, 2014; Lombriser et al. 2013; Puchwein, Baldi & Springel 2013; Arnold, Puchwein & Springel 2015; Cataneo et al. 2016; Arnalte-Mur, Hellwing & Norberg 2017), the properties of voids (Zivick et al. 2015; Cautun et al. 2018), cluster properties (Lombriser et al. 2012a,b; Arnold, Puchwein & Springel 2014), redshift-space distortions (Jennings et al. 2012), and velocity dispersions of dark matter (DM) haloes (Schmidt 2010; Lam et al. 2012; Lombriser et al. 2012b). Weak gravitational lensing in $f(R)$ gravity has been investigated as well (Shirasaki, Hamana & Yoshida 2015; Shirasaki et al. 2017; Li & Shirasaki 2018). Hydrodynamical simulations studied the Sunyaev–Zel'dovich effect and the temperature in galaxy clusters (Arnold et al. 2014; Hammami et al. 2015) and the Lyman $\alpha$ forest (Arnold et al. 2015) in $f(R)$ gravity. High-resolution studies of galaxy clusters (Corbett Moran, Teyssier & Li 2014) and Milky Way-sized haloes (Arnold, Springel & Puchwein 2016) have been performed as well employing zoomed simulation techniques. In addition, cosmological simulations have been used to calibrate scaling relations for the dynamical mass of galaxy clusters in $f(R)$ gravity (Mitchell et al. 2018) that incorporate the non-linearities introduced by the chameleon screening mechanism.

In this work, we introduce the largest simulations, in terms of particle number, of $f(R)$ gravity. Employing $2048^3$ simulation particles in boxes of 768 and 1536 $h^{-1}$ Mpc sidelength we performed a set of four simulations in total for the $|\overline{f_{R0}}| = 10^{-5}$ (F5) gravity model and a $\Lambda$ cold dark matter ($\Lambda$CDM) cosmology for comparison. Along with several time slice outputs the simulations feature continuous 2D and 3D light-cone outputs that are dedicated to enable clustering and lensing analysis on the light-cone in $f(R)$ gravity at a so far unreached precision. Similar studies employing large-box high-resolution simulations with a light-cone output for $\Lambda$CDM cosmologies have been carried out previously by the MICE collaboration (Crocce et al. 2015; Fosalba et al. 2015a,b).

This paper is the first of a series of papers analysing the simulations. It focuses on very high-resolution studies of power spectra and correlation functions of both DM and haloes, halo mass functions and halo concentrations and linear halo bias. Making use of the different simulation box sizes a resolution study for cosmological simulations in $f(R)$ gravity is carried out as well. We also present a first result on weak lensing, although a more detailed study of weak gravitational lensing will be carried out in future work.

This paper is structured as follows. In Section 2, we introduce the theory of $f(R)$ gravity and the chameleon mechanism and the Hu & Sawicki (2007) model. A brief introduction to the simulation code and the simulations carried out within this project is given in Section 3. Section 4 presents our results that are finally discussed and summarized in Section 5.

## 2 $f(R)$ GRAVITY

$f(R)$ gravity is a widely studied modified gravity model (Schmidt 2010; Li et al. 2012; Puchwein et al. 2013; Llinares et al. 2014) that allows to explain the late-time accelerated expansion of the universe without a cosmological constant $\Lambda$. Given its compatibility with the recently observed speed of gravitational waves (Abbott et al. 2017; Ezquiaga & Zumalacárregui 2017), it has also become a very important testbed for deviations from GR.

$f(R)$ gravity is an extension of GR. It is constructed by adding a scalar function $f(R)$ to the Ricci scalar $R$ in the action of standard gravity (Buchdahl 1970):

$$S = \int \mathrm{d}^4x \sqrt{-g} \left[ \frac{R + f(R)}{16\pi G} + \mathcal{L}_\mathrm{m} \right], \tag{1}$$

where $g$ is the determinant of the metric $g_{\mu\nu}$, $G$ is the gravitational constant, and $\mathcal{L}_\mathrm{m}$ is the Lagrangian of the matter fields. By varying the action with respect to the metric one obtains the field equations of (metric) $f(R)$ gravity, the so-called *modified Einstein equations*:

$$G_{\mu\nu} + f_R R_{\mu\nu} - \left( \frac{f}{2} - \Box f_R \right) g_{\mu\nu} - \nabla_\mu \nabla_\nu f_R = 8\pi G T_{\mu\nu}. \tag{2}$$

The $\nabla$ signs denote covariant derivatives with respect to the metric, $\Box \equiv \nabla_\nu \nabla^\nu$, $T_{\mu\nu}$ is the energy–momentum tensor associated with the matter Lagrangian, $R_{\mu\nu}$ is the Ricci tensor, and $f_R \equiv \mathrm{d}f(R)/\mathrm{d}R$ is the derivative of the scalar function with respect to the Ricci scalar.

For cosmological simulations in standard gravity one commonly works in the Newtonian limit of GR, i.e. assumes weak fields and a quasi-static behaviour of the matter fields. This assumption is also adopted for most modified gravity simulations (including this work). Its limitations in the context of $f(R)$ gravity are discussed in Sawicki & Bellini (2015). In the Newtonian limit, the 16-component equation (2) simplifies to two equations: a *modified Poisson equation*,

$$\nabla^2 \Phi = \frac{16\pi G}{3} \delta\rho - \frac{1}{6} \delta R; \tag{3}$$

and an equation for the so-called scalar degree of freedom $f_R$,

$$\nabla^2 f_R = \frac{1}{3} \left( \delta R - 8\pi G \delta\rho \right). \tag{4}$$

$\Phi$ denotes the total gravitational potential, $\delta\rho = \rho - \bar{\rho}$ is the perturbation to the background density $\bar{\rho}$, and $\delta R$ is the perturbation to the background value of the Ricci scalar, i.e. the background curvature.

In order to simulate cosmic structure formation one has to choose a specific functional form $f(R)$. In order to be consistent with current observational data, the model should respect observational limits on deviations from GR in our local environment and should lead to a cosmic expansion history that is similar to that in a $\Lambda$CDM cosmology. For this work, we adopt a model that was designed to

meet these requirements (Hu & Sawicki 2007):

$$f(R) = -m^2 \frac{c_1 \left(\frac{R}{m^2}\right)^n}{c_2 \left(\frac{R}{m^2}\right)^n + 1}, \tag{5}$$

where $m^2 \equiv \Omega_{\rm m} H_0^2$ and $c_1$, $c_2$, and $n$ are parameters of the theory. Throughout this work, we adopt $n = 1$. If one sets $\frac{c_1}{c_2} = 6\frac{\Omega_\Lambda}{\Omega_{\rm m}}$ and $c_2 \frac{R}{m^2} \gg 1$, the theory closely reproduces the expansion history of a ΛCDM universe. In the latter limit, the derivative of equation (5) can be simplified to

$$f_R = -n \frac{c_1 \left(\frac{R}{m^2}\right)^{n-1}}{\left[c_2 \left(\frac{R}{m^2}\right)^n + 1\right]^2} \approx -n \frac{c_1}{c_2^2} \left(\frac{m^2}{R}\right)^{n+1}. \tag{6}$$

The remaining free parameter of the theory is now fully described by the background value of the scalar field $f_R$ at redshift $z = 0$, $\bar{f}_{R0}$. With a suitable choice of this parameter $f(R)$ gravity recovers GR in high-density regions that is necessary to be consistent with solar system tests through the associated chameleon mechanism (Hu & Sawicki 2007). An overview of current constraints on $\bar{f}_{R0}$ can be found in Terukina et al. (2014). Within this work we adopt F5, which is in slight tension with local constraints unless there is significant environmental screening by the Local Group. As we aim to test gravity on much larger scales it is nevertheless still a valuable model to study. Given its slightly stronger deviation from GR compared to models that fully satisfy Solar system constraints (such as $|\bar{f}_{R0}| = 10^{-6}$), it can lead to important insights into how the deviations affect large-scale cosmological measures such as weak lensing and clustering statistics. In order to fully explore the GR testing capacities of upcoming large-scale structure surveys like *Euclid* (Laureijs et al. 2011) or LSST (LSST Science Collaboration 2009), it is critically important to gain a detailed understanding of how these measures are altered by possible modifications to gravity.

## 3 SIMULATIONS AND METHODS

Employing the cosmological simulation code MG-GADGET (Puchwein et al. 2013), we carry out a set of four collisionless cosmological simulations. Each of the simulations runs once for the F5 model and once for a ΛCDM cosmology using identical initial conditions. The first pair of simulations contains $2048^3$ simulation particles in a $1536\,h^{-1}$ Mpc sidelength simulation box, the second pair has the same number of particles in a $768\,h^{-1}$ Mpc sidelength box, reaching mass resolutions of $M_{\rm part} = 4.5 \times 10^9$ and $3.6 \times 10^{10}\,h^{-1}\,{\rm M}_\odot$, respectively. All of the runs use the Planck Collaboration et al. (2016) cosmology with $\Omega_{\rm m} = 0.3089$, $\Omega_\Lambda = 0.6911$, $\Omega_{\rm B} = 0.0486$, $h = 0.6774$, $\sigma_8 = 0.8159$, and $n_{\rm s} = 0.9667$.

MG-GADGET is based on the cosmological simulation code P-GADGET3. It is capable of running both hydrodynamical and collisionless simulations in the Hu & Sawicki (2007) $f(R)$ gravity model. For the simulations presented in this work, we use the local time stepping scheme for modified gravity that is described in detail in Arnold et al. (2016). In the following we will give a brief overview of the functionality of the code (a more comprehensive description is given in Puchwein et al. 2013).

In order to solve equation (4) for the scalar degree of freedom, MG-GADGET uses an iterative Newton–Raphson method with multigrid acceleration on an adaptively refining mesh (adaptive mesh refinement, AMR, grid). To avoid unphysical positive values for $f_R$ that can occur due to numerical values in the simulations, the code solves for $u = \log(f_R/f_{R0})$ instead of computing $f_R$ directly (this trick was first applied by Oyaizu 2008). Once the solution for $f_R$ is known, one can use it to calculate an effective mass density that accounts for all $f(R)$ gravity effects including the chameleon mechanism:

$$\delta\rho_{\rm eff} = \frac{1}{3}\delta\rho - \frac{1}{24\pi G}\delta R. \tag{7}$$

By adding this effective density to the real mass density, the total gravitational acceleration can now in principle be obtained using the standard TREE-PM Poisson solver that is implemented in P-GADGET3. In order to allow for local time stepping, the standard and the modified gravity accelerations are nevertheless calculated separately for the short range (tree-based) forces (see Arnold et al. 2016 for a more detailed description of the local time stepping in MG-GADGET).

All four simulations feature a 2D light-cone output consisting of 400 HEALPix[1] maps (Górski et al. 2005) between redshift $z = 80$ and 0. The maps are equally spaced in lookback time and have a resolution of 805 306 368 pixels. Using the 'Onion Universe' approach (Fosalba et al. 2008), they are constructed as follows: if the simulation reaches a redshift $z = z_i$ at which a light-cone output is desired, the simulation box is repeated several times in all directions such that the whole volume up to the distance corresponding to the redshift $z_i$ around an imaginary observer is covered (see Fig. 1). Subsequently all simulation particles contained in a thin spherical

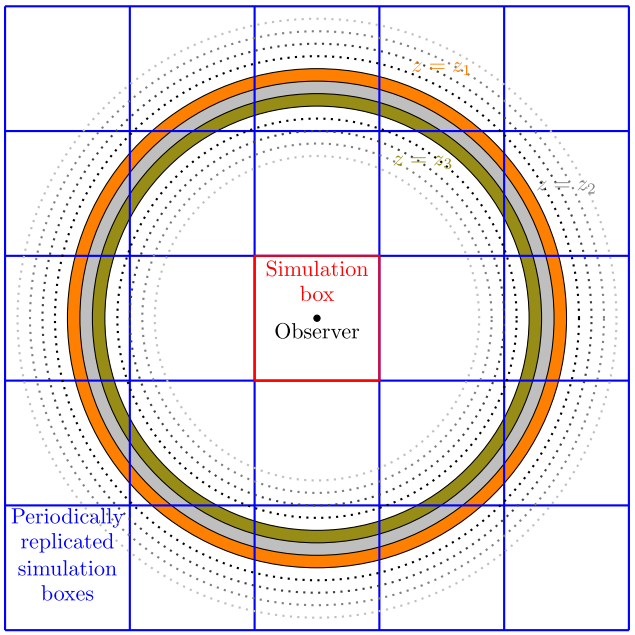


**Figure 1.** Illustration of the method used to construct the full-sky light-cone output. The 400 2D light-cones are equally spaced in lookback time. For each output, the simulation box is periodically replicated several times in each direction and all particles contained in a thin spherical shell (around an imaginary observer) corresponding to the simulation redshift $z = z_i$ are selected. The selected particles are projected onto a 2D HEALPix density map. The thickness $\Delta z$ of the shells is chosen such that they completely cover the volume up to redshift $z = 80$. This approach minimizes the repetition of structure in the light-cone. For output times $z < 1.4$, the full 3D position information (for the $1536\,h^{-1}$ Mpc simulations) or a 3D friends-of-friends (FoF) halo catalogue (for the $768\,h^{-1}$ Mpc simulations) is stored as well.

[1] http://healpix.sourceforge.net/

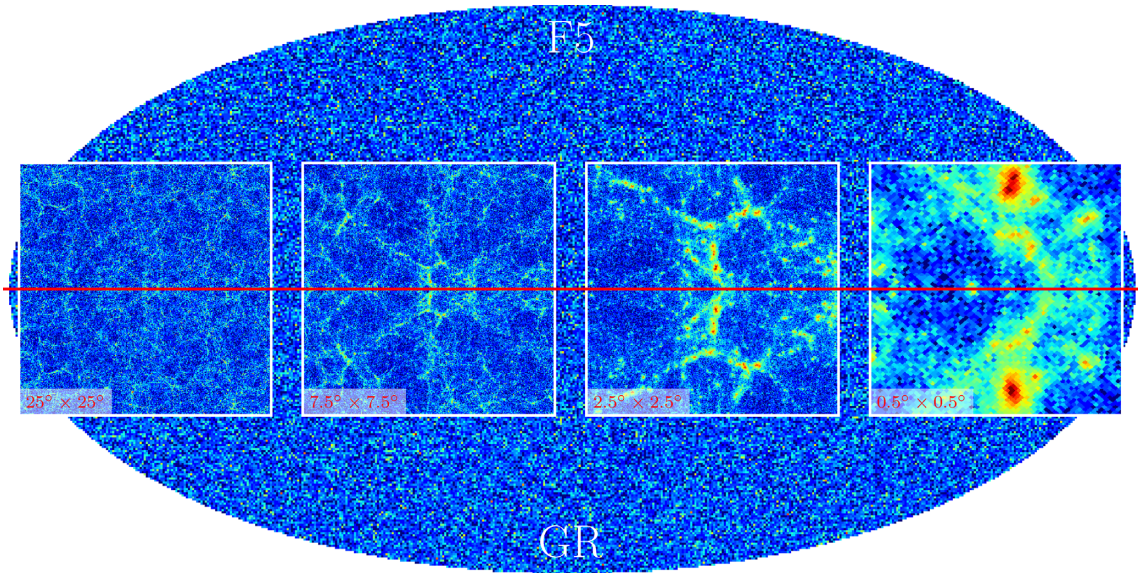


**Figure 2.** A full-sky HEALPix map in Mollweide projection for $z = 0.5 \pm 0.01$ from the $768\,h^{-1}$ Mpc simulation box produced by stacking the 2D light-cone output for the given redshift interval. The upper half of the map shows the F5 simulation output, the lower half shows the output from the simulation in ΛCDM cosmology. The squared maps are zoomed visualizations of the central region of the maps in both theories with a sidelength of 25°, 7.5°, 2.5°, and 0.5°.

shell around $z_i$ are selected and binned onto the HEALPIX map. The thickness of the shells is chosen such that the light-cone output is space filling.

Along with the 2D light-cone output the $1536\,h^{-1}$ Mpc simulation boxes feature a full 3D light-cone output between $z = 1.4$ and 0 that is constructed by storing the full 3D position data for all the selected particles within the shell around $z_i$ at a given output time. For the $768\,h^{-1}$ Mpc simulations, a 3D halo catalogue on the light-cone is produced on the fly instead of the 3D position output. The centres of the haloes are identified using a shrinking sphere approach for all objects identified by the friends-of-friends (FoF) halo finder of P-GADGET3. Along with their position several properties such as their mass, velocity, centre of mass, and tensor of inertia are stored.

In addition to the light-cones, the simulation output features several time slices and halo catalogues obtained with the SUBFIND algorithm (Springel et al. 2001).

## 4 RESULTS

In order to illustrate the 2D light-cone output of the simulations, Fig. 2 shows a stacked HEALPix density map around redshift $z = 0.5$ in Mollweide projection. The map was produced from the $768\,h^{-1}$ Mpc simulation box for both the F5 (upper half) and a ΛCDM (lower half) model. Dark blue regions correspond to low matter densities, lighter colours to regions with higher matter densities, while the highest densities are indicated by dark red regions. The squared maps are zoomed projections of the central region of the maps in both cosmological models. The maps for the GR model are mirrored along the red line, i.e. they show the same spatial regions as the maps for $f(R)$ gravity. One can see from the zooms that the density field on large scales is only mildly altered by $f(R)$ gravity, while some differences appear on small scales. In order to perform a more quantitative study of this, we will consider matter and halo clustering statistics below.

### 4.1 Matter and lensing power spectra

The DM power spectrum obtained from the simulations is shown in Fig. 3. In order to calculate power spectra over a larger range of scales without performing computationally expensive fast Fourier transform (FFT) for high-resolution grids the density field was folded onto itself twice to obtain the power spectrum at small scales (see Springel et al. 2018, for a more detailed description of the method). To avoid noise due to the lack of modes at the large-scale end of the spectrum, a correction factor for the low-$k$ spectrum was calculated from the initial conditions and used to correct the cosmic variance errors in the power spectra at later times. To ensure that the power spectrum is measured correctly on small scales, we subtract a constant shot-noise correction term from the spectrum.

The left-hand panels of Fig. 3 show the absolute values of the power spectrum at $z = 0$ and 1. The right-hand panels give the relative difference of the $f(R)$ gravity power spectra with respect to ΛCDM. As expected from previous works $f(R)$ gravity influences the power spectrum mainly in the regime of non-linear structure growth (Oyaizu, Lima & Hu 2008; Li et al. 2013; Puchwein et al. 2013; Arnold et al. 2015). The relative difference between GR and the F5 model increases with increasing $k$. As the background absolute value of the scalar degree of freedom, $|\bar{f}_R(a)|$, decreases with increasing redshift, one expects a smaller influence of $f(R)$ gravity on the power spectrum at higher redshifts. This is well consistent with the results presented in the plot. At $z = 1$, the relative difference reaches about 7 per cent at $k = 1\,h\,\mathrm{Mpc}^{-1}$ but grows to roughly 18 per cent for $z = 0$ at the same scale. Note that, although we do not provide statistical error bars (largely dominated by sample variance in most of the scales shown) for our measurements, we are mainly interested in relative differences or the ratio between F5 and GR, for which sample variance approximately cancels out.

In order to verify the simulation results, the relative difference in the power spectrum is compared to results from the Modified Gravity Code Comparison Project (Winther et al. 2015, orange dotted lines in the right-hand panels of Fig. 3). The results are in very

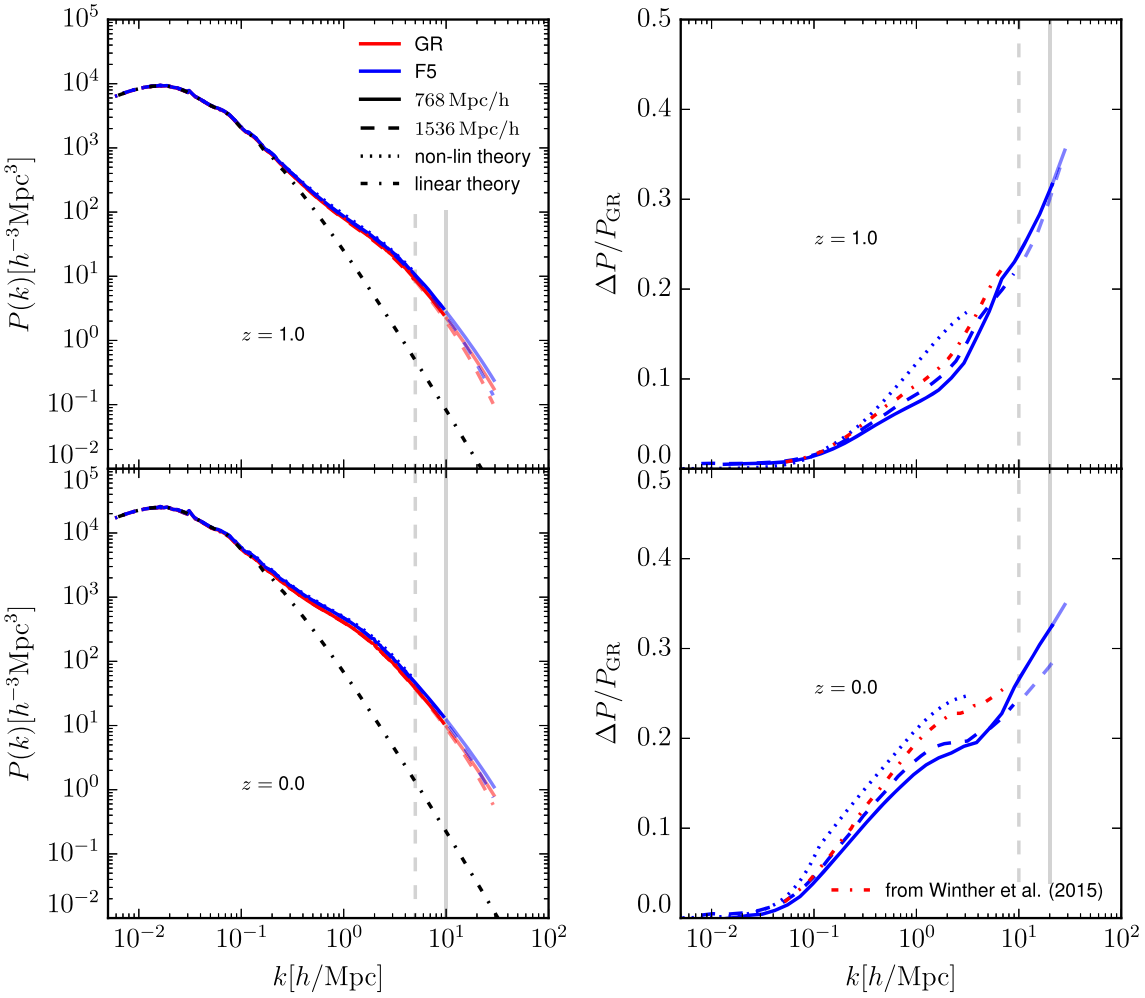


**Figure 3.** The matter power spectrum at $z = 1$ (top panels) and $z = 0$ (bottom panels) for a ΛCDM (red) and a F5 universe (blue). Solid lines refer to results of the $768\,h^{-1}$ Mpc simulations, dashed lines refer to the $1536\,h^{-1}$ Mpc simulation boxes. Numerically converged results are shown as vivid lines, results shown as faint lines might be affected by resolution. The resolution limits are also indicated by the grey vertical dashed and solid lines for the large and small simulation boxes, respectively. The dotted lines show non-linear theory predictions from HALOFIT (Takahashi et al. 2012) and MG-HALOFIT (Zhao 2014) for standard gravity and an $f(R)$ universe, respectively. Dash–dotted lines display the linearly evolved initial power spectrum. The right-hand panels display the relative difference of the F5 simulations to the ΛCDM reference simulations. The dotted lines indicate the relative difference predicted by HALOFIT and MG-HALOFIT. The dash–dotted orange lines show the results from Winther et al. (2015).

good agreement with the relative differences in the power spectra presented in this work. The small differences at the 1–2 per cent level are well within the variations expected due to cosmic variance, different resolutions, and slightly different cosmological parameters (Li et al. 2013).

In Fig. 4, we present a resolution study for the power spectrum of Fig. 3. The plot shows the relative difference between the power spectra measured from the large and the small simulation boxes for both the $f(R)$ gravity simulations and a ΛCDM universe. As one can see from the plot, the spectra of different box size simulations agree within ∼2 per cent up to $k = 5\,h\,\mathrm{Mpc}^{-1}$ for both models at $z = 0$ and within ∼4 per cent for $z = 1$ and the same $k$-range. We therefore conclude that the absolute value of the matter power spectrum can be trusted up to $k = 5\,h\,\mathrm{Mpc}^{-1}$ for the $1536\,h^{-1}$ Mpc simulation boxes and up to $k = 10\,h\,\mathrm{Mpc}^{-1}$ for the $768\,h^{-1}$ Mpc simulation boxes reflecting the factor of 2 spatial resolution difference. We indicate the range over which we trust the spectrum with the vivid coloured lines in Fig. 3. The results shown by the faint lines should be treated with caution.

Although the range where the absolute values of the power spectrum are trustworthy is quite restricted, Fig. 4 shows that both gravity models are affected in a very similar way towards the high-$k$ end of the plot. The relative difference between the modified gravity power spectra and those for the ΛCDM models will therefore be reliable until a larger value of $k$ that we estimate to be $k = 10\,h\,\mathrm{Mpc}^{-1}$ for the large simulation box. This conclusion is furthermore supported by the agreement between the results of the 768 and $1536\,h^{-1}$ Mpc simulation boxes in the right-hand panels of Fig. 3 up to $k = 10\,h\,\mathrm{Mpc}^{-1}$. The results from the small boxes can thus be trusted up to $k = 20\,h\,\mathrm{Mpc}^{-1}$. Again, we plot the converged results as vivid lines, while results shown as transparent lines might be affected by resolution.

As one can easily see in the right-hand panels of Fig. 3, the relative difference in the matter power spectrum due to the modifications of gravity is consistent between the 1536 and the $768\,h^{-1}$ Mpc simulation box within the converged range in $k$. The results are still consistent between the two simulations at different resolutions for $k = 1\,h\,\mathrm{Mpc}^{-1}$. At $z = 0$, they nevertheless deviate significantly

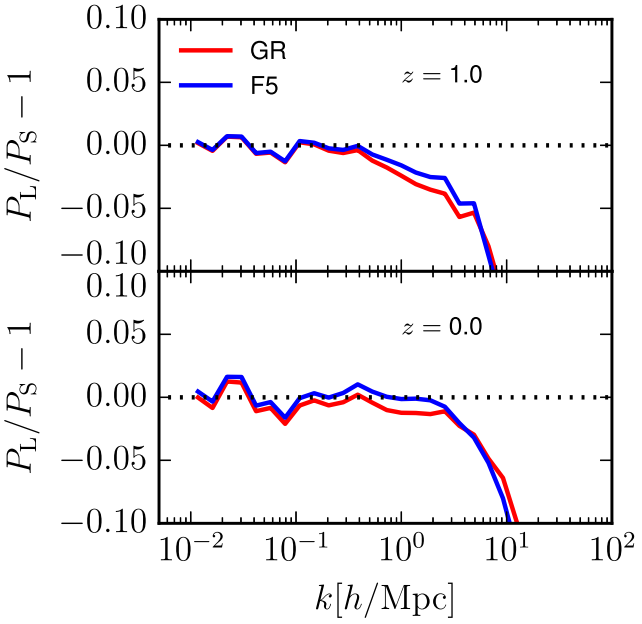


**Figure 4.** The relative difference of the power spectra in the $1536\,h^{-1}$ Mpc simulation box ($P_L$) with respect to the power spectra in the $768\,h^{-1}$ Mpc simulation box ($P_S$) for a ΛCDM cosmology (red lines) and F5 (blue lines). The upper panel shows the comparison for $z = 1$, the lower panel for $z = 0$. Dotted black lines indicate equality.

above $k = 10\,h\,\mathrm{Mpc}^{-1}$. This deviation might be caused by an increased, unphysical screening towards the resolution limit of the AMR grid in the simulations.

To compare our findings for the matter power spectrum to non-linear theory predictions derived with the HALOFIT (Takahashi et al. 2012) and MG-HALOFIT (Zhao et al. 2009; Hojjati, Pogosian & Zhao 2011; Zhao 2014) codes for a ΛCDM and a $f(R)$ gravity universe, respectively, we plot these predictions in Fig. 3 as well. The predictions provide a good fit to our simulation data for the relative difference at the low-$k$ end of the plot, while small differences appear towards larger values of $k$. Note that these predictions have been calibrated on simulation results and thus we choose to show them only where these are well converged (Takahashi et al. 2012; Zhao 2014).

Fig. 5 shows the power spectrum at the baryon acoustic oscillation (BAO) scale with respect to different reference power spectra for $z = 1$ and 0. The panels on the left-hand side display the power spectrum divided by the smoothed power spectrum in order to make the BAOs visible. The results for the $1536\,h^{-1}$ Mpc simulation boxes have been shifted vertically for clarity. The solid black lines (also shifted) show the fluctuations in the initial power spectrum used to create the initial conditions for the simulations linearly evolved to the redshift of the plots. As one can see in the figure, the results for $f(R)$ gravity match the results for the ΛCDM model very well. There is thus negligible influence of $f(R)$ gravity on the growth of the BAO fluctuations. All differences are induced by non-linear structure formation and affect primarily smaller scales. This conclusion is confirmed by the right-hand panels of the plot, showing the power spectrum divided by the linearly evolved initial power spectrum. Note that additional statistical fluctuations in the small box results due to the lack of large-scale modes with respect to the larger box simulation.

It has been noted in previous works that the relative difference in the power spectrum between $f(R)$ gravity and ΛCDM is of the same order as the relative difference induced by baryonic feedback processes in full-physics hydrodynamical simulations (Puchwein et al. 2013). Using the ultrahigh-resolution simulations performed for this work and state-of-the-art hydrodynamical simulations like those carried out within the EAGLE (Schaye et al. 2015) and IllustrisTNG (Naiman et al. 2018; Nelson et al. 2018; Pillepich et al. 2018; Springel et al. 2018) projects we review this degeneracy in Fig. 6. We show the relative difference between the F5 simulations and the ΛCDM reference runs (blue lines) in comparison to the changes induced by baryons on the total (dashed lines) and the DM (solid lines) power spectrum (the values are from Springel et al. 2018). As one can spot from the plot, the relative difference between the DM power spectrum in a full-physics hydrodynamical simulation and a DM-only run is much smaller than the difference due to $f(R)$ gravity. The total matter power spectrum is nevertheless suppressed by 20–25 per cent at scales of $k \approx 20\,h\,\mathrm{Mpc}^{-1}$ due to baryonic feedback. The plot therefore suggests that the effects due to baryons and $f(R)$ gravity would approximately cancel at this scale.

According to the hydrodynamical simulations considered here, the influence of baryons on the power spectrum is on the other hand negligibly small at scales around $k = 1\,h\,\mathrm{Mpc}^{-1}$. There might thus be a sweet spot for testing $f(R)$ gravity at these scales with upcoming large-scale structure surveys. *Euclid* will e.g. map the DM distribution up to $k = 5\,h\,\mathrm{Mpc}^{-1}$ (Laureijs et al. 2011), where we measure sizeable deviations (≈20 per cent) in F5 models relative to ΛCDM. As a cautionary remark, we nevertheless have to add that the increased forces in $f(R)$ gravity can themselves influence feedback processes. Fully conclusive statements can therefore only be drawn from simulations that include both baryonic feedback and $f(R)$ gravity at the same time. One also has to keep in mind that the influence of baryons on the power spectrum is still relatively uncertain (Vogelsberger et al. 2014; Schaye et al. 2015; Springel et al. 2018) and depends on a number of tuneable feedback parameters. It might therefore well be that power spectra of both $f(R)$ gravity and ΛCDM cosmology can be brought into agreement with observations by changing the simulation parameters.

As a cautionary remark we note that in addition to the degeneracies in the matter power spectrum between baryonic feedback and modified gravity, there are a number of additional effects that can influence the power spectrum, particularly at small scales. Massive neutrinos can for example suppress structure formation on small scales and therefore counterbalance the $f(R)$ gravity influences on the power spectrum (Baldi et al. 2014; Peel et al. 2018). An additional complication is introduced by the accuracy of power spectra computed from numerical simulations. While the relative difference between theories of modified gravity and GR in the power spectrum can be assessed very accurately (Winther et al. 2015), the absolute values of the spectra (i.e. the observable quantity) are still uncertain to a few per cent on scales $k > 1\,h\,\mathrm{Mpc}^{-1}$.

The 2D HEALPix light-cone output allows us to compute the angular power spectrum at different redshifts. The results are presented in Fig. 7, showing the power at $z = 0.5$, 1, and 1.5 in the upper panels and the corresponding differences between the spectra in the F5 simulations and ΛCDM in the lower panels. The behaviour is similar to the 3D power spectrum. The influence of $f(R)$ gravity grows with decreasing redshift. At $z = 1.5$, the relative difference reaches roughly 7 per cent at a multipole number of $l = 10^4$. At the same scale, the relative difference grows to 15 per cent at $z = 1$ and further increases to 25 per cent at redshift 0.5. This result is consistent with what we measured for the 3D $P(k)$. In the Limber limit, there is a

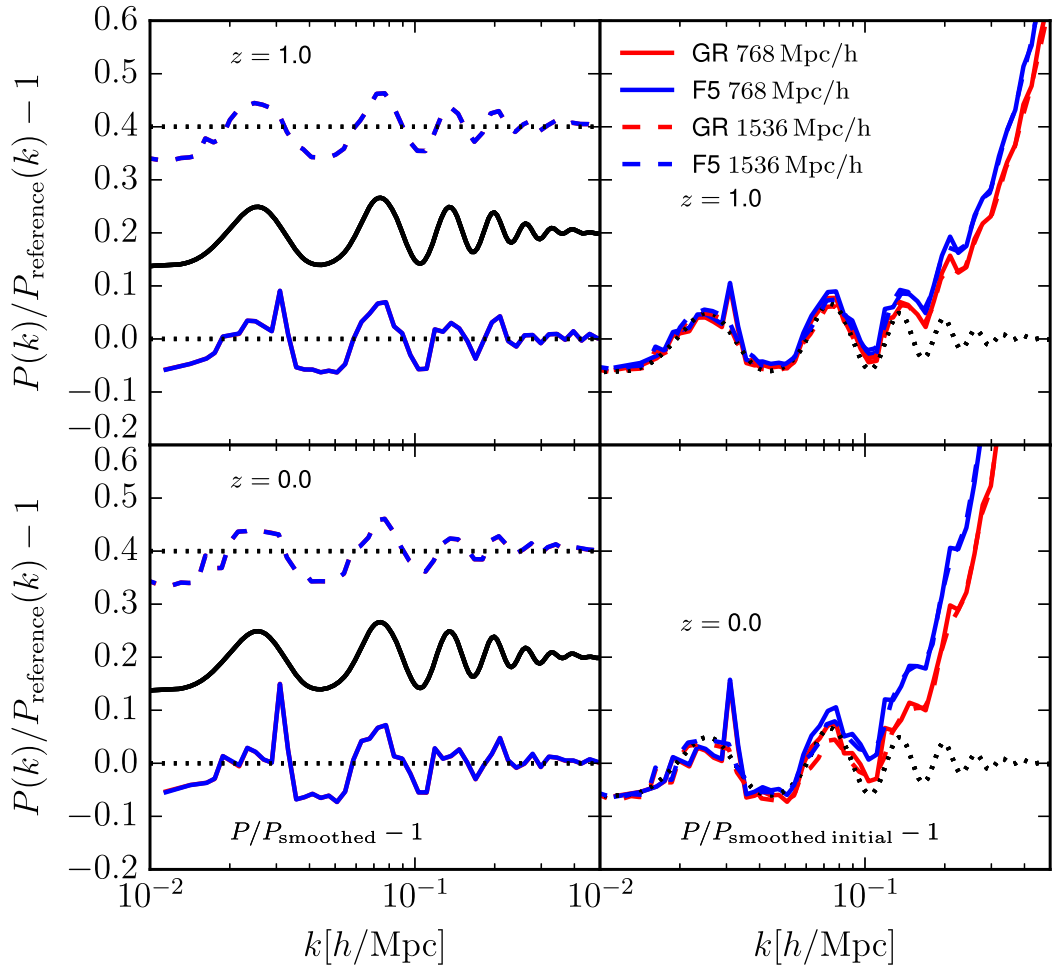


**Figure 5.** The relative difference of the matter power spectra in ΛCDM (red lines) and F5 (blue lines) to three different reference power spectra for $z = 1$ (top panels) and $z = 0$ (bottom panels) at the baryon acoustic oscillation (BAO) scale. Solid lines show results from the $768\,h^{-1}$ Mpc simulation box, dashed lines show results from the $1536\,h^{-1}$ Mpc simulation box. The left-hand panels display the matter power spectrum with respect to the smoothed matter power spectrum. The results for the large box have been shifted vertically for clarity. Dotted black lines represent equality. The solid black line indicates the position of the BAOs in the initial power spectrum. Note that the results for both cosmologies are identical in the left-hand panels of the plot. The red lines are therefore hidden behind the blue lines. The right-hand panels display the difference of the power spectrum to the smoothed, linearly evolved initial power spectrum. The dotted black lines again indicate the BAOs in the linearly evolved initial power spectrum.

one to one relation between comoving wavenumbers and multipoles at a given redshift $z$, $l = k\,r(z)$. For instance, for $z = 1$, we obtained that F5 exceeded ΛCDM by 15 per cent at $k = 5\,h\,\mathrm{Mpc}^{-1}$, which projects onto $l \approx 10^4$, which is what we observe in the lower central panel of Fig. 7. At lower multipole numbers the effects due to $f(R)$ gravity are smaller. For $z = 0.5$, the increased screening effect due to the lack of resolution at small scales in the $1536\,h^{-1}$ Mpc simulations is also visible in the angular power spectrum: the large simulation boxes show an approximately 4 per cent lower relative difference at $l = 10^4$ compared to the $768\,h^{-1}$ Mpc boxes. As for the 3D matter power spectrum, we compare the simulation results to HALOFIT and MG-HALOFIT predictions. (Note that these are obtained using the Limber approximation.) These provide a very good fit to the absolute values of the angular power on large and intermediate scales as well, while small differences appear at high multipoles around $l \approx 10^4$. Their predictive power for the relative difference between $f(R)$ gravity and ΛCDM universes is nevertheless limited: while HALOFIT/MG-HALOFIT and simulations show reasonable agreement at low $l$, the differences reach up to 5 per cent for larger multipoles.

Continuing the analysis of the 2D light-cone output we show the weak lensing convergence power spectrum in Fig. 8 for sources at redshift $z = 1$. We compare our results from the large and small simulation boxes for both models to linear and non-linear theory predictions for both gravity models in the upper panel of the plot. The relative differences between $f(R)$ gravity and the ΛCDM simulations for both boxes and the theory predictions are shown in the lower panel. The simulation results agree very well between the 768 and the $1536\,h^{-1}$ Mpc simulation box up to $l = 3 \times 10^3$. At smaller angular scales (i.e. larger multipoles), the results start to deviate reaching a 5–10 per cent difference at $l = 10^4$. We thus conclude that the results are converged until $l = 3 \times 10^3$ and there are mass-resolution effects beyond this scale.

The theoretical predictions for GR have been derived using the HALOFIT package (Takahashi et al. 2012). The simulation results are in general in good agreement with the HALOFIT predictions. Above $l = 40$ the fitting formulae are slightly overestimating the lensing convergence power. For the F5 model, we used MG-HALOFIT (Zhao 2014) to derive theoretical predictions. Again, the simulations show a lower lensing convergence power compared to these predictions.

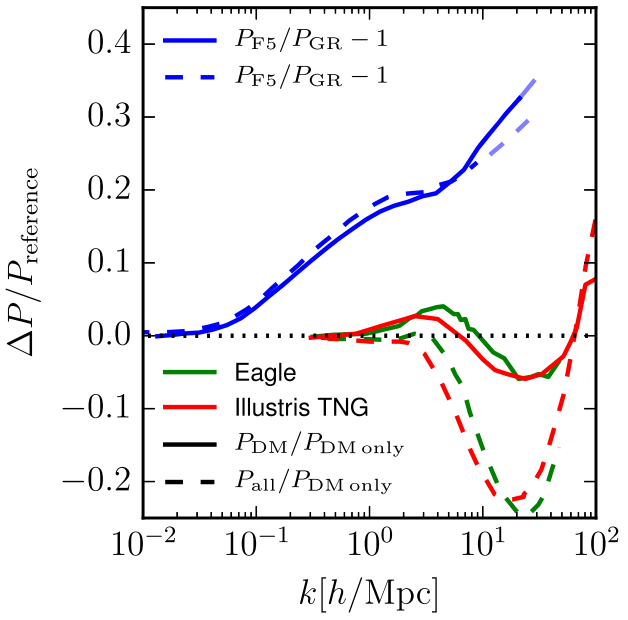


**Figure 6.** The impact of different processes on the matter power spectrum at $z = 0$. The blue lines show the relative difference due to $f(R)$ gravity explored in this work. The effect of baryonic physics on the DM power spectrum in the EAGLE (green; Hellwing et al. 2016) and IllustrisTNG (red; Springel et al. 2018) simulations is indicated by the solid lines. The impact of baryons on the total matter power spectrum is indicated by the green and red dashed lines, respectively. The dotted black line indicates equality.

A similar discrepancy between MG-HALOFIT and simulations has already been observed by Tessore et al. (2015).

As expected from the linear matter power spectrum the relative differences between the modified gravity model and ΛCDM in the lensing convergence are very small at linear scales and increase towards larger multipoles. The results from the large and the small simulation box again agree up to $l = 5 \times 10^3$ and reach a value of 20 per cent at this scale. The main contribution of the 3D DM power to the convergence angular power spectrum for sources at $z = 1$ comes from lenses at $z \approx 0.5$, where we found (see Fig. 3) that the F5 model exceeds ΛCDM by a comparable amount (15–20 per cent) at the corresponding scale given by the Limber limit relation, $k = l/r(z = 0.5) = 5000/1400 \approx 4\,h\,\mathrm{Mpc}^{-1}$. This result is consistent with the findings of Li & Shirasaki (2018). The relative difference between the (MG-)HALOFIT predictions for $f(R)$ gravity and standard gravity is approximately 5 per cent larger than the one measured from the simulations in the non-linear regime, and it drops below the simulation result on higher multipoles.

### 4.2 Halo mass function

The cumulative halo mass function is shown in the upper panels of Fig. 9. The lower panels show the relative difference between the considered modified gravity model and a ΛCDM cosmology. The mass functions have been normalized by volume in order to make the two different simulation box sizes directly comparable. The halo resolution limits given by $m_{halo} > 32 m_{part}$ (the minimum number of particles per group identified by SUBFIND is 32) are indicated in the plot by the solid and dashed vertical grey lines for the small and the large simulation box, respectively. As expected, the large simulation boxes cannot form low-mass haloes due to a lack of

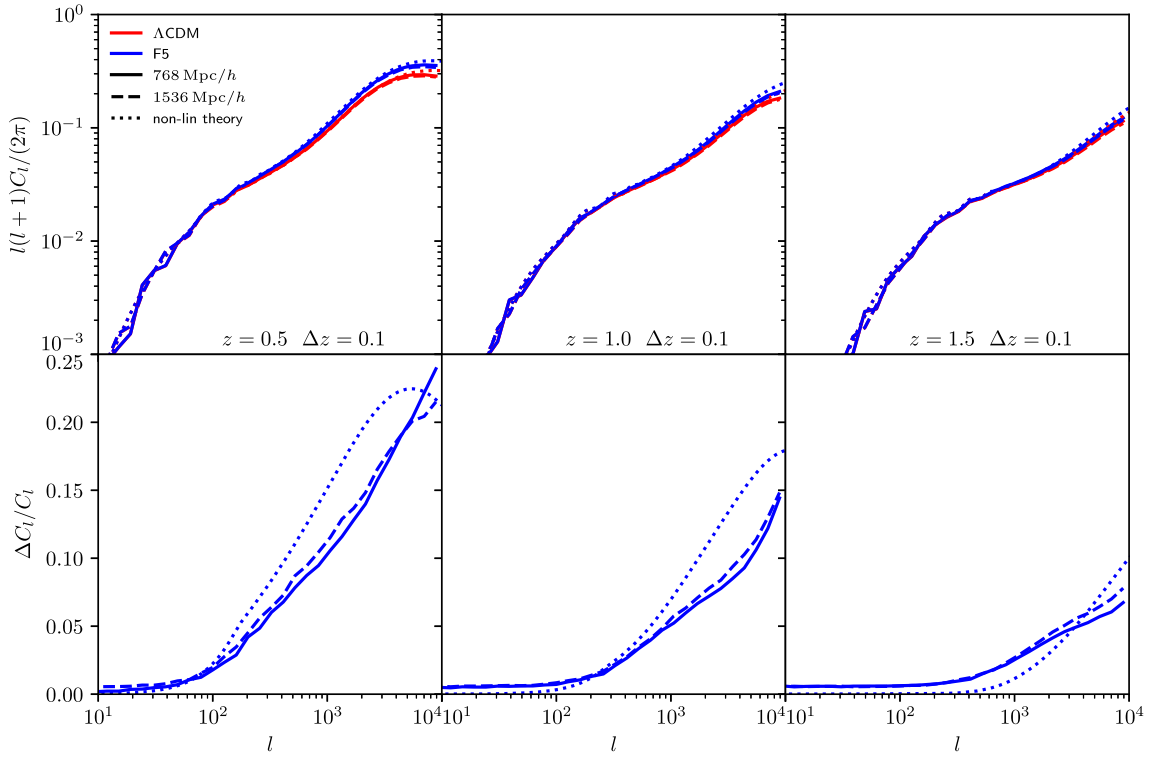


**Figure 7.** Top panels: the angular power spectrum for the $768\,h^{-1}$ Mpc (solid lines) and the $1536\,h^{-1}$ Mpc (dashed lines) simulation boxes for a ΛCDM and a F5 cosmology at $z = 0.5$, 1, and 1.5 (from left to right). Non-linear theory predictions were derived using HALOFIT (Takahashi et al. 2012) and MGHALOFIT Zhao (2014) and are shown as the dotted lines. The bottom panels show the relative difference of the F5 results with respect to a ΛCDM universe.

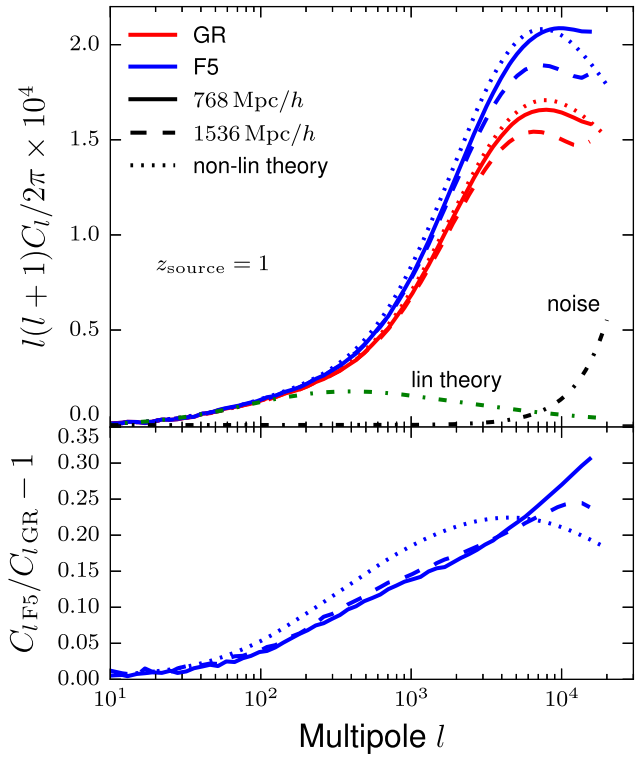


**Figure 8.** The lensing convergence angular power spectrum (top panel) for sources at redshift $z = 0$. Red lines show the results for the ΛCDM cosmology simulations, blue lines for F5. The dashed lines correspond to the power spectra in the $1536\,h^{-1}$ Mpc simulation boxes, the solid lines to results from the $768\,h^{-1}$ Mpc boxes. Non-linear theory predictions were computed using HALOFIT (Takahashi et al. 2012) and MGHALOFIT (Zhao 2014) for standard gravity and an $f(R)$ universe, respectively (dotted lines). Linear theory predictions are indicated by the green dash–dotted line. The black dash–dotted line indicates the shot-noise level for the $1536\,h^{-1}$ Mpc simulation box. The relative differences between $f(R)$ gravity and ΛCDM for the two boxes and the non-linear theory predictions are displayed in the bottom panel.

resolution. The curves for the $1536\,h^{-1}$ Mpc boxes therefore do not reach the low-mass end of the plot. The $768\,h^{-1}$ Mpc simulations on the other hand cannot form haloes with masses above $3 \times 10^{15}\,{\rm M}_\odot$ because of the limited volume.

The mass functions are enhanced in $f(R)$ gravity with respect to GR. The relative difference between the models reaches 25 per cent at $\approx 10^{13}\,{\rm M}_\odot$ for redshift $z = 1$. The difference decreases towards lower and higher masses. At $z = 0$, the relative difference has a maximum at $\approx 10^{14}\,{\rm M}_\odot$. This behaviour is consistent with what one would expect from the evolution of the background value of the scalar field $\bar{f}_R(a)$.

At high redshift, the background value of the scalar field is smaller (see e.g. Arnold et al. 2014). The mass threshold for screening is therefore lower and $f(R)$ gravity mainly affects lower mass haloes. These haloes will consequently grow faster and become more massive leading to more intermediate-mass haloes in the mass function, compared to GR. Towards lower redshift, the mass threshold for screening shifts towards higher masses, while the intermediate-mass haloes at the same time continue growing faster than in GR. The peak in the mass function will consequently shift towards higher masses with decreasing redshift.

The results for the halo mass function are also consistent with those found in Winther et al. (2015). Both the relative differences found in this work and in Winther et al. (2015) are smaller than those reported in Schmidt et al. (2009), who considered the mass function in $f(R)$ gravity using $M_{300\,\rm crit}$ as opposed to $M_{200\,\rm crit}$ that is used in this work. As the density in the central part of the haloes is higher in $f(R)$ gravity compared to a ΛCDM model (Arnold et al. 2016), a larger difference in the mass function using $M_{300\,\rm crit}$ is reasonable. It is worth noting that the simulations employed in this work have both better mass resolution and larger box sizes compared to these previous works. We can therefore analyse the mass function over a much wider range of scales and with significantly better statistics.

Comparing the relative difference between the analytical fitting functions to the difference between the modified gravity model and GR simulations it is obvious that the theoretical uncertainties are much bigger than those induced by the gravity model. The gap between theoretical predictions and simulations is much larger than the difference between the gravitational theories themselves. Comparing the relative difference between the analytical fitting functions we find that the Tinker et al. (2010) predictions fit our simulation results very well. The Sheth et al. (2001) fitting formula works reasonably well at $z = 1$ and for small halo masses at $z = 0$ but does not describe the present-day mass function in the simulations very well at the high-mass end. We also note that the gap between theoretical predictions and simulations is much larger than the difference between the gravitational theories themselves. The <25 per cent change in halo abundance, corresponds to only a small shift on the mass axis. Given uncertainties in halo mass measurements, it thus seems very challenging to use halo mass functions for constraining the deviations from GR considered here.

### 4.3 Matter and halo correlation functions

Fig. 10 shows the DM two-point correlation function for the four simulations at redshift $z = 1$ and 0. The correlation functions are calculated in real space employing the gravity tree of MG-GADGET. The right-hand-side panels display the relative difference between the F5 model and a ΛCDM universe. As for the quantities considered above, the impact of $f(R)$ gravity is larger on small scales. At $z = 0$, the relative difference reaches about 35 per cent at scales of $r = 10^{-2}\,h^{-1}$ Mpc, decreases roughly linearly in $\log(r)$ and reaches zero at $r \approx 10\,{\rm Mpc}\,h^{-1}$. For redshift $z = 1$, the relative difference due to modified gravity at small scales is approximately the same. It nevertheless decreases faster towards large scales reaching $\Delta\xi/\xi_{\rm GR} = 0$ at $r \approx 1\,{\rm Mpc}\,h^{-1}$. The relative difference between $f(R)$ gravity and GR is smaller for the large simulation boxes at small scales. This effect is caused by the unphysical flattening of the correlation functions once the spatial resolution limit of the simulations is approached (we use a gravity softening of 0.01 and $0.02\,h^{-1}$ Mpc for the small and the large simulation boxes, respectively).

The halo–halo two-point correlation functions were analysed by splitting the halo sample identified by SUBFIND into six different $m_{200\,\rm crit}$ mass bins for all four simulations performed within this project. The mass bins are selected such that they span at least 0.5 dex in mass, but also contain at least $10^5$ haloes to ensure sufficiently low noise. The resulting bin-boundaries are $\log(m\,{\rm M}_\odot^{-1}\,h) = 11$–11.5, 11.5–12, 12–12.5, 12.5–13, 13–13.5, and 13.5–14. Fig. 11 shows these autocorrelation functions for three of the mass bins at redshift $z = 1$. Relative differences between standard and $f(R)$ gravity are displayed in the lower panels. The results for the intermediate- (centre panel) and the high-mass bin (right-hand panel) shown in the plot are consistent between the 768 and $1536\,h^{-1}$ Mpc simulation boxes. We do not show the results of the large box simulations in the left-hand panel

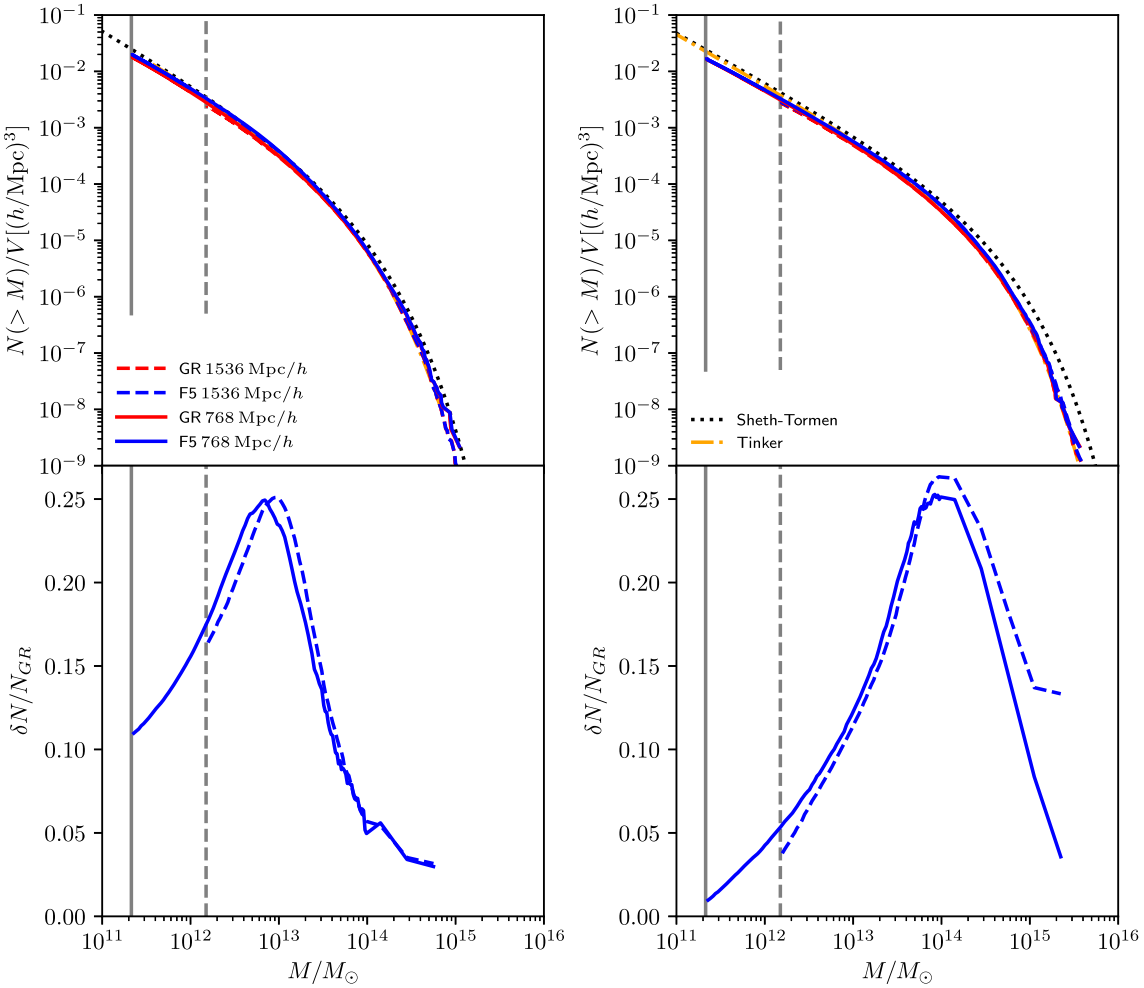


**Figure 9.** The cumulative dark matter (DM) halo mass function at $z = 1$ (left-hand panels) and $z = 0$ (right-hand panels). Solid lines refer to the 768 $h^{-1}$ Mpc simulations, dotted lines to the 1536 $h^{-1}$ Mpc runs. The bottom panels show the relative difference between F5 and ΛCDM. The vertical solid and dashed lines indicate the halo resolution limit for the 768 and 1536 $h^{-1}$ Mpc simulation box, respectively. Analytical predictions using the methods of Tinker et al. (2010) and Sheth, Mo & Tormen (2001) are shown as the orange dash–dotted lines and black dotted lines, respectively.

as the two lowest mass bins are below the halo mass-resolution limit shown in Fig. 9. At small radii, the halo two-point correlation functions are affected by the finite size of the haloes, limiting the minimal distance between two haloes of a given mass. This effect is especially pronounced for larger mass haloes whose distance is limited by (twice) their radius. The correlation functions in the intermediate- and the high-mass bin therefore decrease towards lower radii and cannot be used as a meaningful cosmological observable at these length scales.

The relative difference in correlation between $f(R)$ gravity and the ΛCDM simulations does not show a strong dependence on radius or mass in Fig. 11. The haloes are about 10 per cent less correlated in $f(R)$ gravity compare to GR at both the high- and the low-mass end of the halo mass function in our simulations, while the relative difference is about 7 per cent in the high-resolution simulation for intermediate masses. The relative difference in correlation functions from the big simulation box slightly decreases with increasing radius in this mass bin, from about 5 per cent at low radii to no significant difference at large radii. This effect is likely caused by the limited mass resolution of the 1536 $h^{-1}$ Mpc simulation box. We therefore think that the results from the small simulation box are more reliable for this mass bin.

Fig. 12 displays the same quantities at redshift $z = 0$. Halo–halo correlation functions are again shown for three of the mass bins in the upper panels, while the corresponding relative differences are plotted in the lower panels. The results from the 1536 $h^{-1}$ Mpc simulation box are again not shown for the lowest mass bin. As for $z = 1$, the correlation functions for the other mass bins are consistent between the two independent simulations of different mass resolution. The relative differences between the modified gravity simulations and standard cosmology are of the order of 10 per cent. They nevertheless show a slight dependence on radial scale that is most pronounced at low halo masses. The relative difference is approximately zero for low radii in the left-hand panel of the plot and decreases to −10 per cent at $r \approx 40$ Mpc $h^{-1}$. As the lowest mass bin is at the resolution limit of the small simulation box, this result should nevertheless be taken with caution. Higher mass haloes are about 8 per cent less correlated in $f(R)$ gravity compared to GR at low radii and show roughly 12 per cent difference at large radii in the plot.

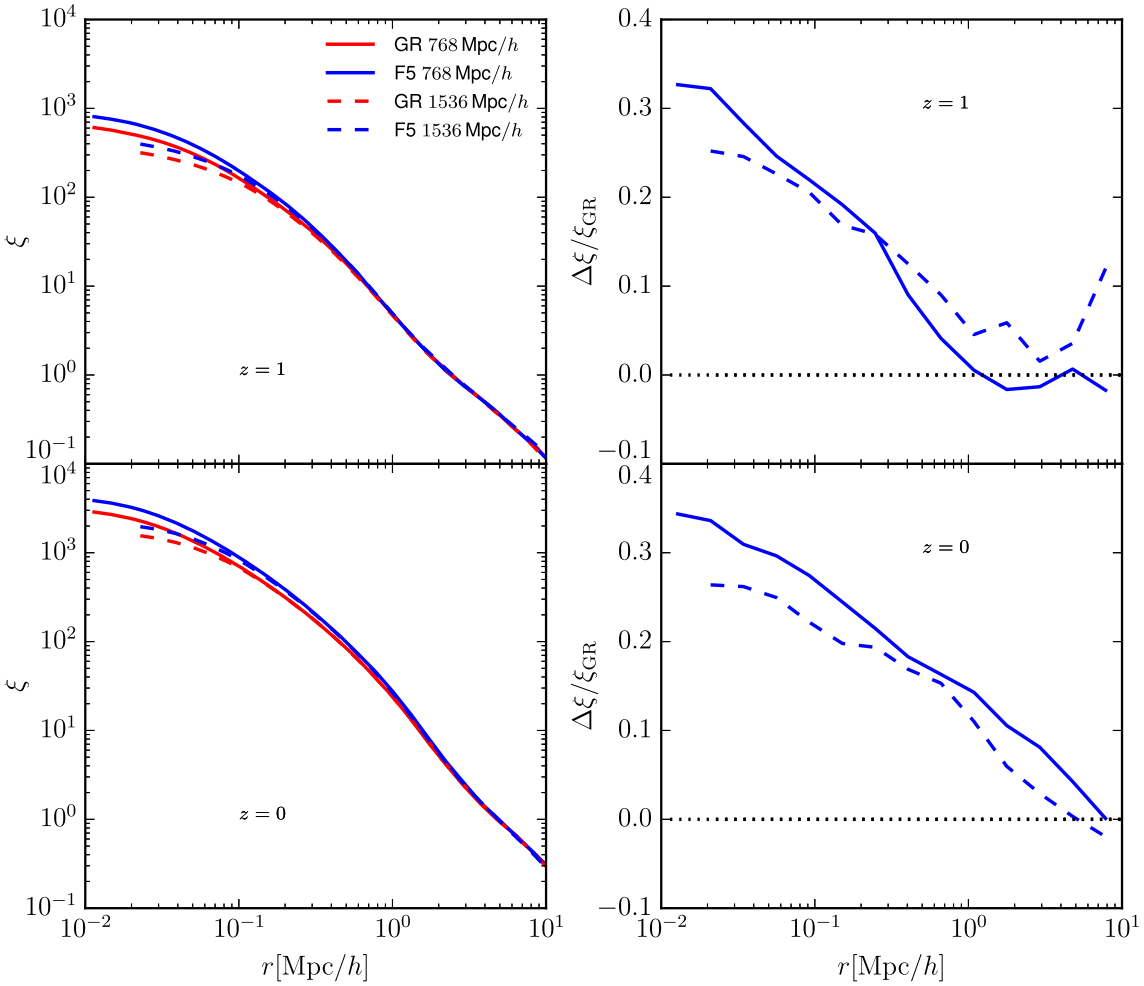


**Figure 10.** The DM two-point correlation function of the two simulation boxes at $z = 0$ and 1 for F5 and ΛCDM cosmologies. The solid lines display results for the 768 $h^{-1}$ Mpc simulation boxes, the dashed lines for the 1536 $h^{-1}$ Mpc runs. The right-hand-side panels show the relative difference of F5 to GR.

### 4.4 Linear halo bias

We define the linear halo bias as $b(m, z)^2 = \xi_{\rm h}(m, z, r)/\xi_{\rm m}(z, r)$, where $\xi_{\rm h}$ is the halo autocorrelation function shown in Figs 11 and 12, and $\xi_{\rm m}$ is the matter autocorrelation function. The halo bias is scale dependent on small scales but asymptotically flattens towards larger radii reaching a constant value at large scales ($r \approx 10\,h^{-1}$ Mpc). This is also visible in the top and middle panels of Fig. 13. While the bias is strongly scale dependent up to $r \approx 3$–$5\,h^{-1}$ Mpc, depending on halo mass, it becomes constant at larger scales. At the large radius end of the plots in Fig. 13, the bias is dominated by the noise that occurs in the matter correlation functions at large scales. These findings are consistent with the results of Crocce et al. (2015, see fig. 16) who find the halo bias to be scale independent at a per cent level for scales larger than 15–20 $h^{-1}$ Mpc in the MICE-GC simulation, with some deviation from scale independence on smaller scales, depending on halo mass. The degree of scale dependence found also depends on the estimator used (halo–matter versus halo–halo correlations). Here, we are primarily interested in the bias in the constant regime, which is usually referred to as *linear halo bias* (Kravtsov & Klypin 1999).

The procedure to obtain the bias is illustrated in Fig. 13 for the same halo mass bins shown in the previous figures (again, we do not show results for the large box in the left-hand panels). The top panels show the (scale dependent) bias for the 768 $h^{-1}$ Mpc simulation boxes. The same quantity is shown for the large boxes in the middle panels. Bottom panels display relative differences between $f(R)$ gravity and a ΛCDM cosmology for both box sizes. In order to obtain the region in which the scale-dependent bias is roughly constant, we calculate its mean over all radii and select radial scales where the bias differs by less than 50 per cent as our fitting region (indicated by the vertical dashed lines in the top and middle panels). Our result for the (scale independent) bias is the median (scale dependent) bias in this region (horizontal dashed lines in the top and middle panels). The relatively large deviations from the mean bias at large and small radii in the plots are caused by the difficulties in measuring correlation functions at these scales, as discussed before. The results for the intermediate- and the high-mass bin for the large and the small simulation box are nevertheless consistent, showing that our results are reliable for these masses.

Fig. 14 shows the results for the scale-independent halo bias as a function of mass and peak height parameter $\nu = \delta_{\rm c}/\sigma(m)$. $\delta_{\rm c} = 1.686$ is the (linearly estimated) critical overdensity for spherical collapse. $\sigma^2(m)$ denotes the variance of the linearly evolved initial density field at $z = 0$ at mass scale $m$. It can be calculated from the convolution of the linear matter power spectrum with a real-space

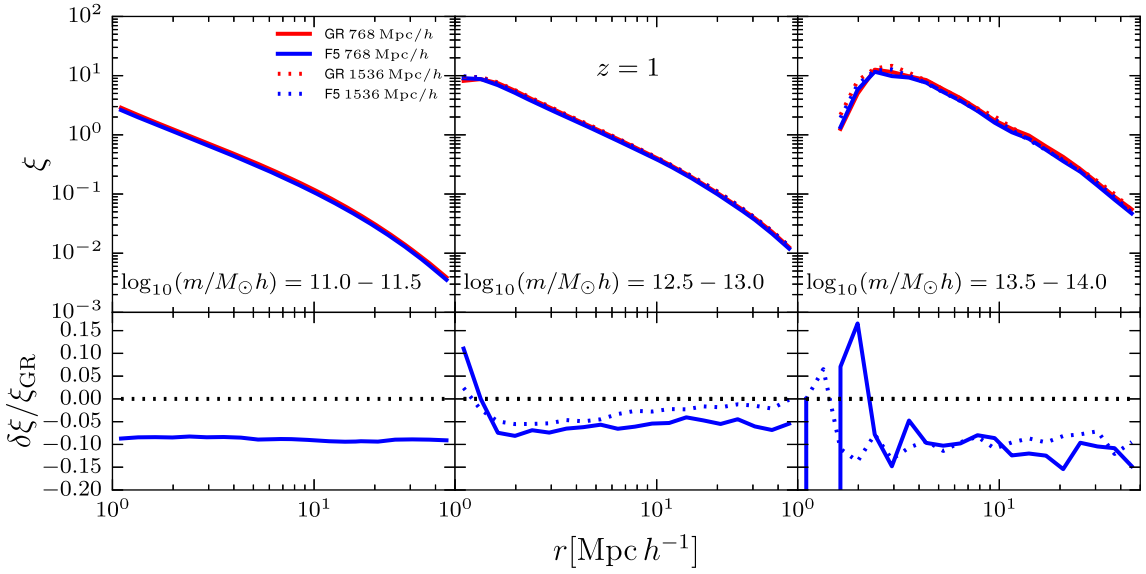


**Figure 11.** The DM halo two-point correlation function at $z = 1$ for a ΛCDM (red) and a F5 (blue) cosmology for three of the six different halo mass ($m_{200\,\mathrm{crit}}$) bins. The solid and dotted lines in the top panels refer to the actual halo autocorrelation function for each mass bin for the 768 and 1536 $h^{-1}$ Mpc simulation boxes, respectively. The relative difference in the halo autocorrelation function between a F5 and a ΛCDM cosmology is displayed in the lower panels for each mass bin, dotted black lines indicate zero relative difference. The results from the large box are not shown in the left-hand panels.

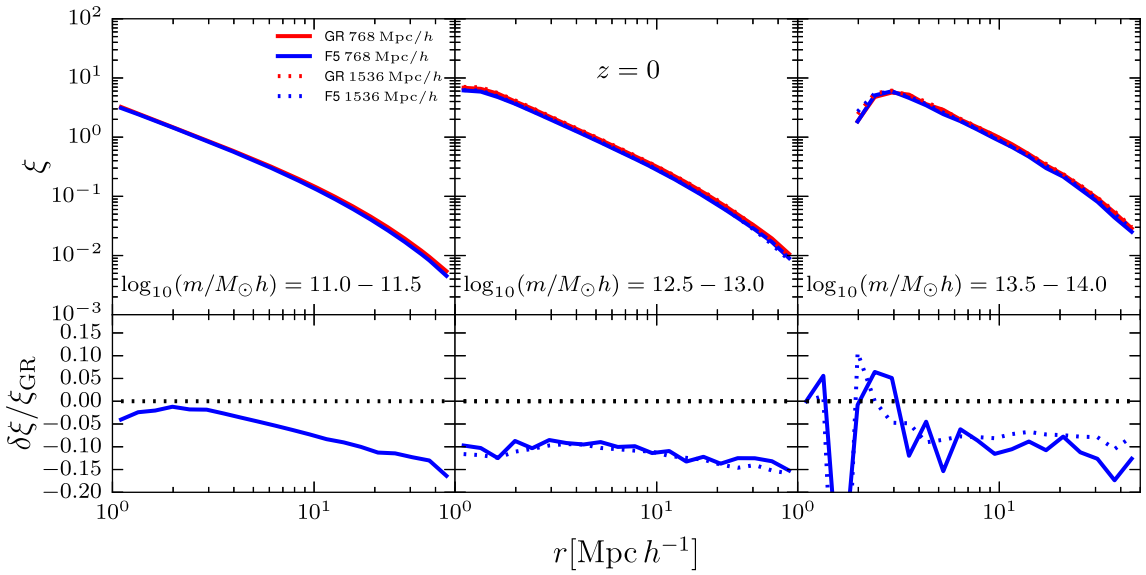


**Figure 12.** Same as Fig. 11, but for $z = 0$.

top hat filter $W_r(k)$ of width $r(m) = (\frac{3m}{4\pi\bar{\rho}})^{1/3}$,

$$\sigma^2(m) = \frac{1}{(2\pi)^3}\int P(k,z)|W_r(k)|^2 4\pi k^2 \mathrm{d}k. \quad (8)$$

The top panels of the plot in Fig. 14 show the bias at redshift $z = 1$ (left) and $z = 0$ (right) for both simulation boxes and models. We restrict the mass range to the well-resolved regions in the simulations. Theoretical predictions from Sheth & Tormen (1999) and Tinker et al. (2010) are shown as the dashed and dotted black lines, respectively.

For all mass bins, the absolute values of the correlation functions agree very well between the simulation boxes. At $z = 1$, the theoretical predictions of Tinker et al. (2010) are well reproduced by our simulations for standard gravity. This is as well the case for $z = 0$. The relative difference between the results from the $f(R)$ gravity and ΛCDM simulations is shown in the lower panels of Fig. 14. The simulations predict 3–5 per cent lower bias in $f(R)$ gravity compared to standard gravity at $z = 0$. This relative difference is lower than the one found in lower resolution simulations by Schmidt et al. (2009). At redshift $z = 1$ the difference in bias seems to depend more strongly on mass. At the low-mass end the relative difference is the same as at $z = 0$, while it drops to a 10 per cent lower bias for $f(R)$ gravity compared to GR at the high-mass end of the plot.

### 4.5 The halo concentration–mass relation

The concentration–mass relation for the DM haloes at $z = 0$ is shown in Fig. 15. The upper panels show the absolute value of the concentration for all four simulations. These inferred from the

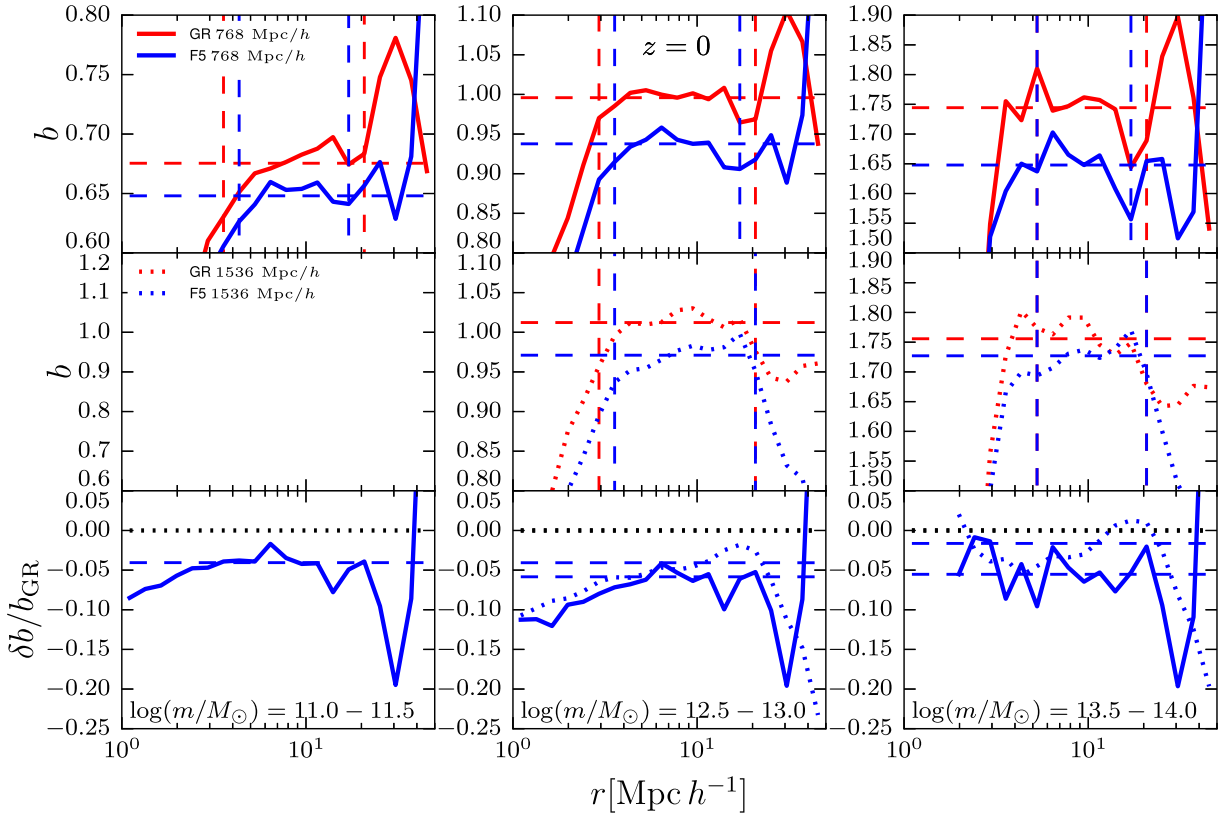


**Figure 13.** The halo bias as a function of distance for ΛCDM (red lines) and F5 (blue lines) cosmologies (top and middle panels) for three of the six different mass bins at $z = 0$. The results in the top panels were obtained from the $768\,h^{-1}$ Mpc simulation box (solid lines), the results in the middle panels from the $1536\,h^{-1}$ Mpc simulations (dotted lines). The dashed horizontal lines indicate the median bias, the dashed vertical lines show the radial range that is used to infer the median bias. The lower panels display the relative difference in the halo bias between F5 and ΛCDM, again using solid and dotted lines for the small and the large boxes, respectively. The dashed lines show the difference of the mean, the black dotted line indicates zero.

circular velocity profile of the haloes using (Springel et al. 2008)

$$\delta_c = 7.213\,\delta_V = 7.213 \times 2\left(\frac{v_{\rm max}}{H_0\, r_{\rm max}}\right)^2,$$

$$\delta_c = \frac{200}{3}\frac{c^3}{\log(1+c) - c/(1+c)}, \tag{9}$$

where $v_{\rm max}$ and $r_{\rm max}$ are the velocity and radius corresponding to the maximum of the profile and $c$ is the concentration parameter. We note that this method can lead to a weakly biased relative difference in the concentration between $f(R)$ gravity and GR compared to profile fitting methods, particularly at the resolution limit of numerical simulations (Baldi & Villaescusa-Navarro 2018). In addition to our simulation results we show theoretical fitting formulas from Neto et al. (2007) and Duffy et al. (2008) (our concentrations are calculated with respect to $r_{200\,\rm crit}$; we therefore choose the corresponding values for the fitting formula from Duffy et al. 2008). In order to be consistent with the analysis in these papers, we show the results for our full halo sample identified by SUBFIND for each of the simulations (left-hand panels) and for relaxed haloes only (right-hand panels). Our criteria for relaxed haloes are the centre-of-mass displacement and submass criterion described in Neto et al. (2007). The centre-of-mass displacement criterion limits the offset between a haloes centre-of-mass and its potential minimum to $0.07 r_{200\,\rm crit}$, while the submass criterion sets an upper bound of 10 per cent on the fraction of halo mass contained in substructures. The lower panels show the relative difference between $f(R)$ gravity and a ΛCDM universe.

As one can see from the upper panels, the Neto et al. (2007) analytical formula provides an excellent fit to our standard gravity simulation results for both the relaxed and the full halo sample. The results for $f(R)$ gravity match the fitting formula as well at the high-mass end of the plot but show more concentrated profiles towards lower masses. At $10^{13.5}\,{\rm M}_\odot\,h^{-1}$, the relative difference reaches 50 per cent for the full sample and 42 per cent for relaxed haloes. This is expected as the stronger forces for unscreened (lower mass) objects in the modified gravity model move mass from the outer regions of the halo towards the centre, leading to a steeper density profile (Arnold et al. 2016). The increased concentration is also consistent with the results shown in Schmidt (2010) and Shi et al. (2015). The deviations of the results from the $1536\,h^{-1}$ Mpc simulation box towards low masses are likely caused by the limited resolution that makes it difficult to identify the maximum of the circular velocity profile.

## 5 SUMMARY AND CONCLUSIONS

We presented the (in terms of particle number) largest simulations of (Hu & Sawicki 2007) $f(R)$ gravity. The set of simulations we analysed consists of four simulations containing $2048^3$ simulation particles each, in 768 and $1536\,h^{-1}$ Mpc boxes for both $f(R)$ gravity and a ΛCDM model. Along with ordinary time slice snapshots the simulations feature 2D and 3D light-cone outputs and FoF and

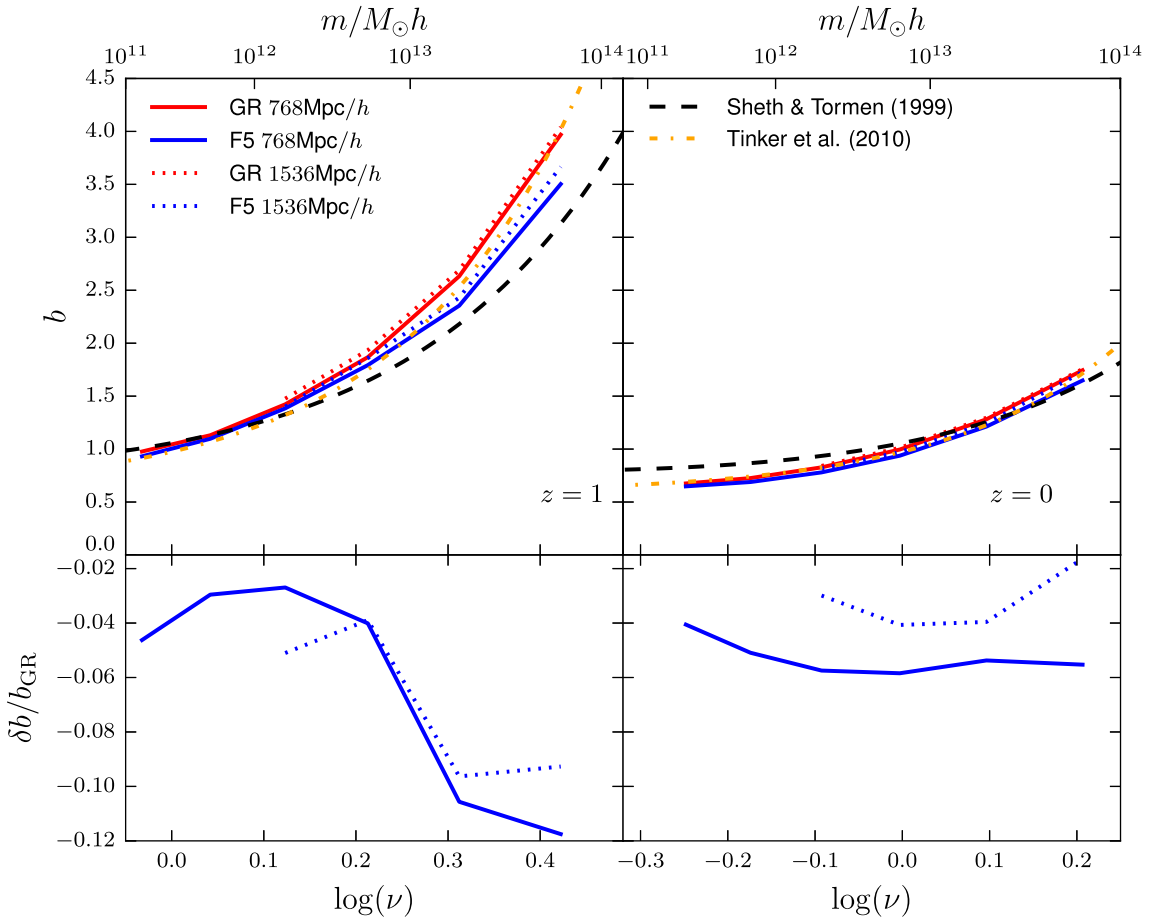


**Figure 14.** The mean halo bias as a function of peak height ($\nu$, lower axis) and mass (upper axis) for F5 (green) and ΛCDM (blue) at $z = 1$ (left-hand panels) and $z = 0$ (right-hand panels). The solid lines with crosses display the results from the small simulation boxes, the dotted lines with +- symbols results from the large volume simulations. Analytical predictions from Sheth & Tormen (1999) and Tinker et al. (2010) are shown as the dashed and dotted black lines, respectively. The lower panels show the relative difference between F5 and ΛCDM.

SUBFIND halo catalogues. We choose F5 as a background parameter for the scalar field for the modified gravity simulations.

Our findings can be summarized as follows.

(i) The matter power spectrum is increased in $f(R)$ gravity on non-linear scales. The relative difference to GR is larger on smaller scales and grows with decreasing redshift. This result is consistent with previous works but extends to a much larger range in $k$. Comparing the power spectra of the two simulations with different resolution, we conclude that the standard and the modified gravity power spectra are affected in a very similar way at the resolution limit of the simulations that makes the relative differences between the different cosmological models trustworthy over a larger $k$-range compared to the absolute values of the individual spectra. The growth of the BAOs is not affected by $f(R)$ gravity. Differences between the gravity models appear only in the non-linear regime. Theoretical predictions for the non-linear matter power spectrum show good agreement with the simulations on large scales. They are nevertheless not accurate enough to precisely predict the relative difference between the cosmological models on smaller scales. The angular power spectrum shows a – within the Limber limit – consistent behaviour.

(ii) The relative difference in the matter power spectrum between $f(R)$ gravity and a ΛCDM universe on small scales ($k \approx 10\,h\,\mathrm{Mpc}^{-1}$) is of the same order of magnitude as the effect of baryonic processes such as feedback from AGN but acts in the opposite direction. Comparing our findings to results of the EAGLE (Hellwing et al. 2016) and IllustrisTNG (Springel et al. 2018) hydrodynamical simulations nevertheless suggests that there is a sweet spot around $k = 1\,h\,\mathrm{Mpc}^{-1}$ where the influence of baryons is very small but $f(R)$ gravity has a sizeable effect on the power spectrum. We note that we cannot make any statement about back-reactions between the two physical processes here. To make a conclusive statement about the interplay of baryonic physics and modified gravity, it will be necessary to include both in one simulation at the same time.

(iii) The changes to the linear and angular power spectrum are reflected in the lensing convergence spectrum. The relative difference in the lensing signal is again larger on smaller scales for the considered modified gravity model and reaches 25–30 per cent on the smallest scales probed by our simulations ($l \approx 10^4$). Our simulation results match the predictions of HALOFIT (Takahashi et al. 2012) and MG-HALOFIT (Zhao 2014) on large scales for the ΛCDM model and $f(R)$ gravity, respectively. On smaller scales the (MG-)HALOFIT predictions overestimate our simulation results. A more detailed analysis of the lensing signal from the light-cone in $f(R)$ gravity is planned in future work.

(iv) The halo mass function is increased for intermediate-mass haloes by about 25 per cent in the considered modified gravity model. Halos at the high- and low-mass end of the correlation

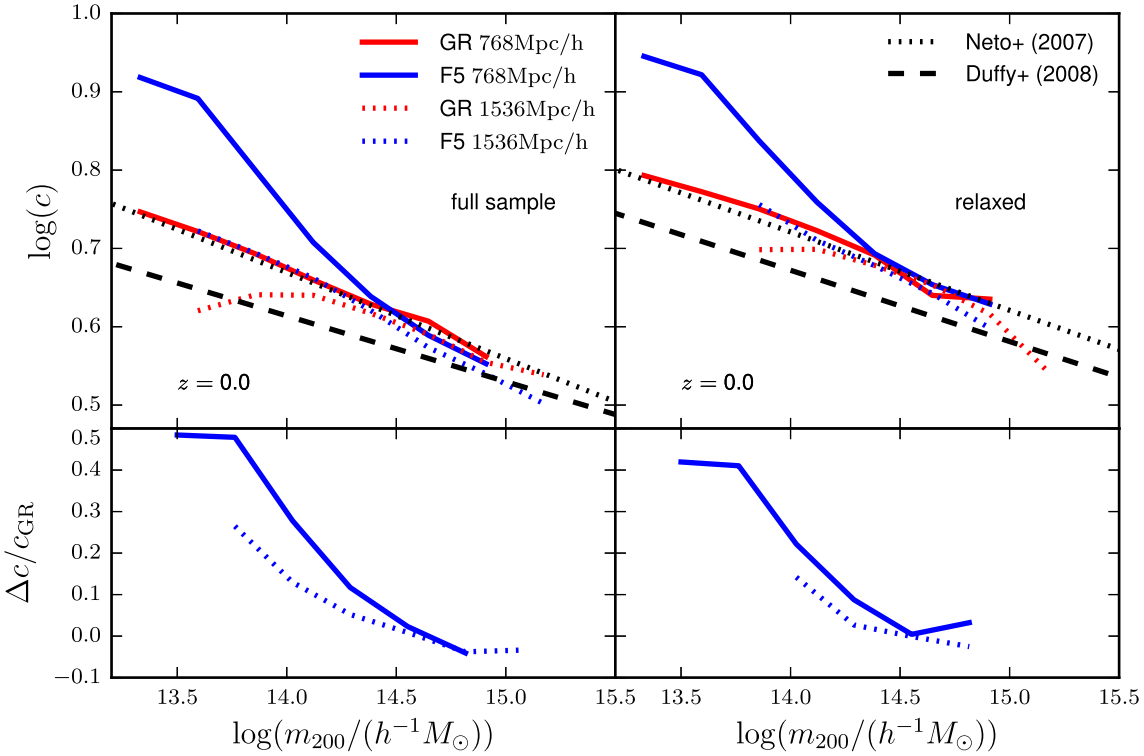


**Figure 15.** The concentration–mass relation for F5 (red) and ΛCDM (blue) at $z = 0$. Concentrations for the full halo sample are displayed in the left-hand panels, concentrations for the relaxed haloes (according to the centre-of-mass displacement and subhalo mass fraction criteria described in Neto et al. 2007) only in the right-hand panels. The dotted lines display results from the 1536 $h^{-1}$ Mpc simulation boxes, the solid lines for the 768 $h^{-1}$ Mpc simulation boxes. The black dotted and dashed lines show analytical fitting formulae from Neto et al. (2007) and Duffy et al. (2008), respectively. The relative difference between F5 and ΛCDM is shown in the lower panels. The concentration is calculated from the maxima of the circular velocity curves obtained with SUBFIND. We only plot bins with an error of the median smaller than 0.02 in $\log(c)$.

function are affected less. The position of the peak in the relative difference between the two gravity models depends on redshift. We observe the maximum relative difference around $10^{13}$ $M_\odot$ at $z = 1$ and around $10^{14}$ $M_\odot$ at $z = 0$. The concentration–mass relation is affected by $f(R)$ gravity as well. While there is no significant difference between the cosmological models for masses above $10^{14.5}$ $M_\odot$ the haloes are more and more concentrated towards lower masses in the modified gravity simulations compared to their ΛCDM counterparts. The relative difference reaches 50 per cent for the full halo sample and 40 per cent for relaxed haloes at masses of $10^{13.5}$ $M_\odot$. The results of our standard gravity simulations are in excellent agreement with the prediction of Neto et al. (2007).

(v) The effects of $f(R)$ gravity on the matter power spectrum is also reflected in the DM autocorrelation function. Matter is more correlated on small scales in modified gravity. The relative differences reach 35 per cent at $r = 10^{-2}$ Mpc $h^{-1}$. In contrast to matter, the DM haloes are less correlated in modified gravity compared to GR. Independent of the mass of the haloes considered the halo–halo correlation function shows roughly 10 per cent lower values in $f(R)$ gravity. The lower halo autocorrelation function results in a lower linear halo bias for modified gravity. Considering this bias as a function of mass we find that our GR results for $z = 0$ and 1 are in good agreement with the Tinker et al. (2010) prediction, while there is a clear difference to the Sheth & Tormen (1999) model. The $f(R)$ gravity simulations predict a lower bias for both redshifts compared to GR. At $z = 1$ the relative difference is mass dependent and drops from 3 per cent at $10^{12}$ $M_\odot$ to 10 per cent at $10^{13.5}$ $M_\odot$. Our $z = 0$ result does not show a clear mass dependence. The simulations predict about 3–5 per cent lower halo bias for this redshift. It is however worth noting that the difference between the models is significantly smaller than the difference between the different theoretical predictions for a ΛCDM universe.

All in all we conclude that the modified gravity light-cone simulation suite provides high resolution, large volume simulation data in $f(R)$ gravity that allows to analyse the effect of modified gravity onto cosmic structure formation over a range of scales unreached so far. The high-resolution light-cone simulations presented in this paper are a valuable tool for exploring possible deviations of modified gravity models with respect to ΛCDM for a wide range of observables. Galaxy mocks based on this set of simulations and their properties will be presented in a forthcoming publication. The results presented in this paper show that the simulations are consistent with previous works and theoretical expectations and show their robustness against mass-resolution effects, indicating that these simulations can be safely used to test gravity using the large-scale distribution of matter and galaxies.

## ACKNOWLEDGEMENTS

The authors like to thank Marco Baldi, Kazuya Koyama, Claudio Llinares, and Baojiu Li for useful discussions and comments. Some of the results in this paper have been derived using the HEALPix (Górski et al. 2005) package.

CA acknowledges support from the European Research Council through ERC-StG-716532-PUNCA. PF acknowledges support from MINECO through grant ESP2015-66861-C3-1-R, and Generalitat de Catalunya through grant 2017-SGR-885. VS acknowl-

edges support from the Deutsche Forschungsgemeinschaft (DFG) through Transregio 33, 'The Dark Universe'. EP acknowledges support by the Kavli Foundation. LB acknowledges the support from the Spanish Ministerio de Economia y Competitividad grant ESP2015-66861.

The simulations performed for this work were run on the Jureca cluster at the Juelich Supercomputing Center in Juelich, Germany, within project HHD29, on Hazelhen at the High-Performance Computing Center Stuttgart in Stuttgart, and on the bwForCluster MLS&WISO Developement. This work used the DiRAC Data Centric system at Durham University, operated by the Institute for Computational Cosmology on behalf of the STFC DiRACHPC Facility (www.dirac.ac.uk). This equipment was funded by BIS National E-infrastructure capital grant ST/K00042X/1, STFC capital grants ST/H008519/1 and ST/K00087X/1, STFC DiRAC Operations grant ST/K003267/1, and Durham University. DiRAC is part of the National E-Infrastructure.

## REFERENCES

Abbott B. P. et al., 2017, ApJ, 848, L13
Arnalte-Mur P., Hellwing W. A., Norberg P., 2017, MNRAS, 467, 1569
Arnold C., Puchwein E., Springel V., 2014, MNRAS, 440, 833
Arnold C., Puchwein E., Springel V., 2015, MNRAS, 448, 2275
Arnold C., Springel V., Puchwein E., 2016, MNRAS, 462, 1530
Baldi M., Villaescusa-Navarro F., 2018, MNRAS, 473, 3226
Baldi M., Villaescusa-Navarro F., Viel M., Puchwein E., Springel V., Moscardini L., 2014, MNRAS, 440, 75
Buchdahl H. A., 1970, MNRAS, 150, 1
Cataneo M., Rapetti D., Lombriser L., Li B., 2016, J. Cosmol. Astropart. Phys., 12, 024
Cautun M., Paillas E., Cai Y.-C., Bose S., Armijo J., Li B., Padilla N., 2018, MNRAS, 476, 3195
Clifton T., Ferreira P. G., Padilla A., Skordis C., 2012, Phys. Rep., 513, 1
Corbett Moran C., Teyssier R., Li B., 2014, preprint (arXiv:1408.2856)
Crocce M., Castander F. J., Gaztañaga E., Fosalba P., Carretero J., 2015, MNRAS, 453, 1513
Duffy A. R., Schaye J., Kay S. T., Dalla Vecchia C., 2008, MNRAS, 390, L64
Ezquiaga J. M., Zumalacárregui M., 2017, Phys. Rev. Lett., 119, 251304
Fosalba P., Gaztañaga E., Castander F. J., Manera M., 2008, MNRAS, 391, 435
Fosalba P., Gaztañaga E., Castander F. J., Crocce M., 2015a, MNRAS, 447, 1319
Fosalba P., Crocce M., Gaztañaga E., Castander F. J., 2015b, MNRAS, 448, 2987
Górski K. M., Hivon E., Banday A. J., Wandelt B. D., Hansen F. K., Reinecke M., Bartelmann M., 2005, ApJ, 622, 759
Hammami A., Llinares C., Mota D. F., Winther H. A., 2015, MNRAS, 449, 3635
Hassan S. F., Rosen R. A., 2012, J. High Energy Phys., 2, 126
Hellwing W. A., Li B., Frenk C. S., Cole S., 2013, MNRAS, 435, 2806
Hellwing W. A., Barreira A., Frenk C. S., Li B., Cole S., 2014, Phys. Rev. Lett., 112, 221102
Hellwing W. A., Schaller M., Frenk C. S., Theuns T., Schaye J., Bower R. G., Crain R. A., 2016, MNRAS, 461, L11
Hojjati A., Pogosian L., Zhao G.-B., 2011, J. Cosmol. Astropart. Phys., 08, 005
Hu W., Sawicki I., 2007, Phys. Rev. D, 76, 064004
Jennings E., Baugh C. M., Li B., Zhao G.-B., Koyama K., 2012, MNRAS, 425, 2128
Joyce A., Jain B., Khoury J., Trodden M., 2015, Phys. Rep., 568, 1
Khoury J., Weltman A., 2004, Phys. Rev. D, 69, 044026
Kravtsov A. V., Klypin A. A., 1999, ApJ, 520, 437
Lam T. Y., Nishimichi T., Schmidt F., Takada M., 2012, Phys. Rev. Lett., 109, 051301
Laureijs R. et al., 2011, preprint (arXiv:1110.3193)
Li Y., Hu W., 2011, Phys. Rev. D, 84, 084033
Li B., Shirasaki M., 2018, MNRAS, 474, 3599
Li B., Zhao G.-B., Teyssier R., Koyama K., 2012, J. Cosmol. Astropart. Phys., 01, 051
Li B., Hellwing W. A., Koyama K., Zhao G.-B., Jennings E., Baugh C. M., 2013, MNRAS, 428, 743
Llinares C., Mota D. F., Winther H. A., 2014, A&A, 562, A78
Lombriser L., Lima N. A., 2017, Phys. Lett. B, 765, 382
Lombriser L., Taylor A., 2016, J. Cosmol. Astropart. Phys., 03, 031
Lombriser L., Schmidt F., Baldauf T., Mandelbaum R., Seljak U., Smith R. E., 2012a, Phys. Rev. D, 85, 102001
Lombriser L., Koyama K., Zhao G.-B., Li B., 2012b, Phys. Rev. D, 85, 124054
Lombriser L., Li B., Koyama K., Zhao G.-B., 2013, Phys. Rev. D, 87, 123511
LSST Science Collaboration, 2009, preprint (arXiv:0912.0201)
Mitchell M. A., He J.-h., Arnold C., Li B., 2018, MNRAS, 477, 1133
Naiman J. P. et al., 2018, MNRAS, 477, 1206
Nelson D. et al., 2018, MNRAS, 475, 624
Neto A. F. et al., 2007, MNRAS, 381, 1450
Nojiri S., Odintsov S. D., 2011, Phys. Rep., 505, 59
Nojiri S., Odintsov S. D., Oikonomou V. K., 2017, Phys. Rep., 692, 1
Oyaizu H., 2008, Phys. Rev. D, 78, 123523
Oyaizu H., Lima M., Hu W., 2008, Phys. Rev. D, 78, 123524
Peel A., Pettorino V., Giocoli C., Starck J.-L., Baldi M., 2018, A&A, 619, A38
Pillepich A. et al., 2018, MNRAS, 475, 648
Planck Collaboration et al., 2016, A&A, 594, A13
Puchwein E., Baldi M., Springel V., 2013, MNRAS, 436, 348
Sakstein J., Jain B., 2017, Phys. Rev. Lett., 119, 251303
Sawicki I., Bellini E., 2015, Phys. Rev. D, 92, 084061
Schaye J. et al., 2015, MNRAS, 446, 521
Schmidt F., 2010, Phys. Rev. D, 81, 103002
Schmidt F., Lima M., Oyaizu H., Hu W., 2009, Phys. Rev. D, 79, 083518
Sheth R. K., Tormen G., 1999, MNRAS, 308, 119
Sheth R. K., Mo H. J., Tormen G., 2001, MNRAS, 323, 1
Shi D., Li B., Han J., Gao L., Hellwing W. A., 2015, MNRAS, 452, 3179
Shirasaki M., Hamana T., Yoshida N., 2015, MNRAS, 453, 3043
Shirasaki M., Nishimichi T., Li B., Higuchi Y., 2017, MNRAS, 466, 2402
Sotiriou T. P., Faraoni V., 2010, Rev. Modern Phys., 82, 451
Springel V., White S. D. M., Tormen G., Kauffmann G., 2001, MNRAS, 328, 726
Springel V. et al., 2008, MNRAS, 391, 1685
Springel V. et al., 2018, MNRAS, 475, 676
Takahashi R., Sato M., Nishimichi T., Taruya A., Oguri M., 2012, ApJ, 761, 152
Terukina A., Lombriser L., Yamamoto K., Bacon D., Koyama K., Nichol R. C., 2014, J. Cosmol. Astropart. Phys., 04, 013
Tessore N., Winther H. A., Metcalf R. B., Ferreira P. G., Giocoli C., 2015, J. Cosmol. Astropart. Phys., 10, 036
Tinker J. L., Robertson B. E., Kravtsov A. V., Klypin A., Warren M. S., Yepes G., Gottlöber S., 2010, ApJ, 724, 878
Vogelsberger M. et al., 2014, Nature, 509, 177
Will C. M., 2014, Living Rev. Relativ., 17, 4
Winther H. A. et al., 2015, MNRAS, 454, 4208
Zhao G.-B., 2014, ApJS, 211, 23
Zhao G.-B., Pogosian L., Silvestri A., Zylberberg J., 2009, Phys. Rev. D, 79, 083513
Zhao G.-B., Li B., Koyama K., 2011, Phys. Rev. D, 83, 044007
Zivick P., Sutter P. M., Wandelt B. D., Li B., Lam T. Y., 2015, MNRAS, 451, 4215

This paper has been typeset from a TEX/LATEX file prepared by the author.